Towards ultracold LiRb molecules

by

Nina Rauhut

Submitted to the Department of Physics
in partial fulfillment of the requirements for the degree of

Diplomarbeit

at the

LUDWIG MAXIMILIANS UNIVERSITÄT MÜNCHEN

August 2007

Signature of the author .....

Department of Physics
August, 1. 2007

Certified by .....

Dr. David J. Jones
Department of Physics, UBC
Thesis Supervisor

Accepted by .....

Privatdozent Dr. Thomas Udem
Max–Planck–Institute for Quantum Optics, LMU

Abstract

This work describes first steps towards the creation and detection of ultracold LiRb molecules, an alkali dimer which thusfar not experimentally investigated despite its highly interesting large permanent electric dipole moment. An operating dual–species magneto–optical trap for Li and Rb was constructed. As part of a large team, my contribution to this success was the design and construction of a pair of water cooled magnetic coils, the vacuum system with the atomic sources for Li and Rb and a time–of–flight mass ion spectrometer. The latter will be employed to directly detect the molecules. Measurements on both the Li and the Rb MOT in order to determine the optimal detuning and field gradient for trapping as many atoms as possible were performed. When this work was completed, the experimental setup was brought to a point, where first photoassociation data is expected to be taken soon.

Contents

List of Tables

List of Figures

Chapter 1

Introduction

The idea to use laser radiation to cool atoms was first proposed by Hänsch and Shawlow [1] and Wineland and Dehmelt [2] in 1975. A paper by Ashkin followed in 1978 [3] in which he described how to slow down a beam of sodium atoms using the radiation pressure of a laser beam. He called this radiative force "scattering force". The most popular atoms for cooling and trapping experiments still are the alkali–metal atoms. First, since the energy difference between the ground and first excited state of all alkali–atoms corresponds to a wavelength which is in the visible or near infra–red region, it is relatively easy to generate the cooling light. Second, their high vapor pressure at modest temperatures makes it easy to design an atomic source just by heating them in an oven or a dispenser. And finally, since all alkali–atoms only have one valence electron, their energy structure is fairly simple. In addition to the alkali atoms, hydrogen and some noble gas atoms have been successfully cooled and trapped.

Since these pioneering experiments, laser cooling has attracted much attention in the scientific community and opened a whole new field of research known as "laser cooling and trapping". At these low temperatures the kinetic energy of the atoms is so small, that they can be trapped and investigated in optical potentials, for example in a standing wave light field (so called optical lattices [4]). At sufficient low temperatures, when the quantum nature of particles become apparent, a remarkable new phenomena called the Bose–Einstein condesation appears, which was predicted by Einstein building upon the work of Bose in 1925 and experimentally realized with rubidium atoms in 1995 [5] leading to a second Nobel Prize (in 2001) awarded to researchers involved with laser cooling and trapping experiments. The first Nobel prize

in this field was awarded to W. Philipps, C. Cohen–Tannoudji and S. Chu in 1997 for demonstrating the principle of laser cooling and optical molasses. Currently, the goal of many researchers is to produce dense samples of ultracold molecules. Molecules are certainly more complicated than atoms – and one might say more interesting – due to their complex internal level structure. This complex internal structure also makes it very difficult, if not impossible, to use standard laser cooling techniques for their creation. Therefore, in recent years, lots of research was done in order to develop molecular cooling schemes. The first ultracold molecules (Cs_2) were created in 1998 [6] via photoassociation, since then all other alkali atoms and some of the heteronuclear alkali dimers (RbCs [7] , LiCs [8], NaCs [9], KRb [10]) have been created via photosassociation. Heteronuclear molecules have attracted particular interest because they are characterized by a permanent electric dipole moment. Applying an external electric field, at ultralow temperatures, the thermal energy of the molecules is much lower than the interaction energy with the field such that their dipole moments can be controlled. The electric dipole moments of cold polar molecules oriented along or against the electric field have been suggested to represent a qbit [12]. Different qbits are coupled by the electric dipole–dipole interaction and an array of these qbits might be used in a quantum computing device. Furthermore, following recent realizations of a moleculear Bose–Einstein condensation [11], the opportunity to create a polar condensate is exciting.

This thesis will be about first steps towards the creation of a sample of ultracold LiRb molecules, a molecule which has not been photoassociated so far. This project is a collaboration project between two laboratories of the Department of Physics of the University of British Columbia: David J. Jones' Laboratory of Ultrafast Femtosecond Spectroscopy and Kirk Madison's Quantum Degenerate Gas laboratory.

The first chapter will give a brief review of the theory of laser cooling and trapping followed by a chapter about the creation of ultracold molecules. Here, in particular, the technique of photoassociation will be discussed and some theoretical aspects related to the LiRb molecule will be presented. The third chapter is devoted to the experimental set–up. In the time period when this work was completed, a dual–species magneto–optical trap for ^{6}Li and ^{85}Rb and/or ^{87}Rb was set up. This chapter contains information on several experimental aspects about how to succesfully set up a MOT: the construction of the vacuum system, the atomic sources, the laser system, the magnetic coils and an attempt of constructing a time–of–flight mass spectrometer to

detect the molecules. Chapter 4 will present some measurements which were performed on the Rb and Li MOT. Unfortunately, the time did not allow to take some photoassociation data, since the laser designated for this process was not ready before the end of this work.

Chapter 2

Cooling and trapping of neutral atoms

2.1 Principle of laser cooling

The fact that a light beam carries momentum and that the scattering of light by an atom produces a force can be used for slowing down an atomic beam. If a laser beam whose frequency is close to resonance with an atomic transition is directed against an atomic ensemble, the laser light is scattered, i.e. photons are absorbed and spontaneously reemitted. The momentum kick that the atoms receive from each scattered photon is quite small, but each atom undergoes this process many times and each photon absorbed tranfers a quantum of momentum $\hbar\vec{k}$ to the atom in the direction of light propagation, where $\vec{k}$ is the wave vector of the laser light. The excited atoms decay spontaneously to the ground state, and although the emitted photon changes the momentum of the atoms, because it occurs in a random direction the momentum transfer from reemission averages to zero after many spontaneous emission events. This process is illustrated in Figure 2.1. The result is a net force acting on the atoms in the direction of light propagation which decelerates the atoms. Since this force is due to the spontaneous emission process, it is refered to as spontaneous force or scattering force.

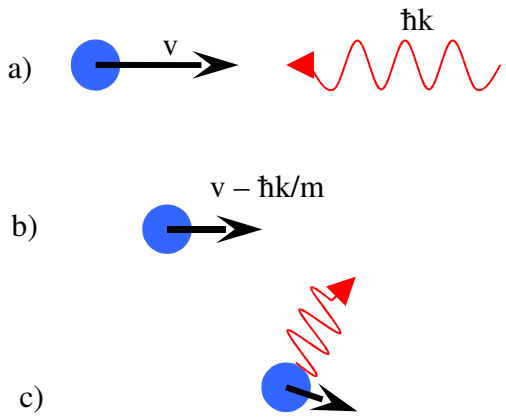

Figure 2.1: (a) An atom with velocity v absorbs a photon with momentum $\hbar k$; (b) The atom is decelerated by $\hbar k/m$; (c) A photon is emitted in a random direction.

2.2 Doppler shifts and optical pumping

A typical velocity change due to one scattering event is about 1 cm/s. Starting with a thermal atomic beam with a mean velocity of about 1000 m/s, it requires 100 000 scattering events to stop the atoms. The time scale for this to happen is in the ms range. Doppler shifts and optical pumping, however, prevent the atoms from coming to a complete stop.

If an atom with velocity $\vec{v}$ moves in the direction opposite to the photons, it will see the laser frequency shifted to the red by an amount $\omega_D = -\vec{k}\cdot\vec{v}$ due to the Doppler effect. In order to maximize the photon scattering rate, the laser light should be detuned by this amount so that its frequency matches the energy difference of the atomic transition. However, the atoms to be cooled, have a Boltzmann distribution in velocity. Therefore, only a small portion of the atoms is in resonance with the laser beam. Furthermore, since these atoms repeatedly absorb photons and therefore slow down as desired, the Doppler shift changes and after a while these atoms are not in resonance anymore and the decceleration process stops. This is not an effective cooling, because only a few atoms are deccelerated over a small time range. One of

the solutions to avoid this problem would be to continuously change the frequency of the laser (chirping) so that the light interacts with an ensemble of atoms with a wide distribution in velocity. Another solution is to change the energy level separation and therefore the resonance frequency by applying an inhomogeneous magnetic field. The beam is then called a Zeeman slowed beam, since the change of resonance frequency is due to the Zeeman effect . Using the arrangement described so far it would still not result in an efficient cooling due to optical pumping effects. Until now, the atoms were assumed to be two level systems. The ground state as well as the excited state of the atoms might be split by the hyperfine interaction into states with energy differences larger than the optical linewidth of the laser. The total angular momentum $\vec{F}$ is then given by $\vec{F} = \vec{I} + \vec{J}$ where $\vec{J} = \vec{L} + \vec{S}$ is the sum of the orbital momentum $\vec{L}$ and the spin momentum $\vec{S}$, and $\vec{I}$ is the nuclear spin momentum. In the case of alkali atoms the ground state consists of three hyperfine levels with $|I - \frac{1}{2}| \leq F \leq I + \frac{1}{2}$. An excited atom can relax by spontaneous emission to any of the hyperfine states of the ground state and is then so far out of resonance with the laser light that it cannot be reexcited and therefore does not experience any force. A straight forward solution to this problem of optical pumping is the use of a second laser with a frequency tuned to the transition between this "dark" state and an excited state. As a consequence, the atoms get excited and can decay back to the original ground state where they are in resonance again with the laser light and are decelerated.

2.3 Optical molasses

If laser beams hit the atoms from all six room directions, all atoms – no matter in which direction they move – are slowed down. This arrangement of laser fields is called 'optical molasses'. An optical molasses will cool atoms, however, the atoms will still diffuse out of the intersection region of the cooling beams.

The average force acting on the atoms is given by the photon scattering rate times the momentum of a photon.

$$scattering\ force = photon\ momentum\ \times\ scattering\ rate$$

The scattering rate can be obtained by solving the optical Bloch equation for the steady state [13]. The scattering force is then given by

$$\vec{F}_{\text{scatt}} = \hbar\vec{k}\gamma = \hbar\,\vec{k}\,\frac{\Gamma}{2}\,\frac{I/I_0}{1 + I/I_0 + [2(\delta - \vec{k}\cdot\vec{v})/\Gamma]^2} \tag{2.1}$$

where the first factor $\hbar\vec{k}$ is the momentum transfer for each photon and the second factor γ is the scattering rate. Here, Γ is the natural linewidth of the excited state, I is the light intensity, I_0 is the saturation intensity and δ is the detuning from resonance. Eq. (2.1) is valid for low light intensities, so that stimulated emission events can be neglected. The scattering rate increases with increasing light intensity until it reaches the upper limit of $\Gamma/2$ when the atom divides its time equally between ground and excited state.
For an optical molasses in the one dimensional case, where only two counterpropagating laser beams are used to cool atoms, the total force on the atoms, F_{OM}, is then given by the sum of the scattering forces from each of the beams, thus

$$F_{\text{OM}} = \hbar\,k\,\frac{\Gamma}{2}\,\frac{I/I_0}{1 + I/I_0 + [2(\delta - kv)/\Gamma]^2} - \hbar\,k\,\frac{\Gamma}{2}\,\frac{I/I_0}{1 + I/I_0 + [2(\delta + kv)/\Gamma]^2} \tag{2.2}$$

For small velocities v and low intensities I such that $I/I_0 << 1$ this expression can be approximated by

$$\vec{F}_{\text{OM}} = 2\hbar k^2 \frac{(2I/I_0)(2\delta/\Gamma)\vec{v}}{[1 + (\frac{2\delta}{\Gamma})^2]^2} = -\alpha\vec{v} \tag{2.3}$$

where terms of order $(kv/\Gamma)^4$ and higher have been neglected. If $\delta < 0$, this force opposes the velocity, resulting in viscous damping with damping coefficient α. This is where the name "optical molasses" comes from. Figure 2.2(a) shows the force from each of the beams (red and green line) as well as the total force (blue line) as a function of velocity for a detuning $\delta = -\Gamma$ and a saturation parameter $I/I_0 = 2$. At zero velocity the force is zero and is linear over a range of velocities on the order of Γ/k. Figure 2.2(b) shows the same force but this time as a function of detuning for a saturation parameter $I/I_0 = 2$ and a velocity $v = 0.5\,\frac{\Gamma}{k}$. For positive detunings the force is positive and therefore has the same direction as the velocity. Only negative detunings result in a force which opposes the velocity of the atoms and therefore deccelerates them.

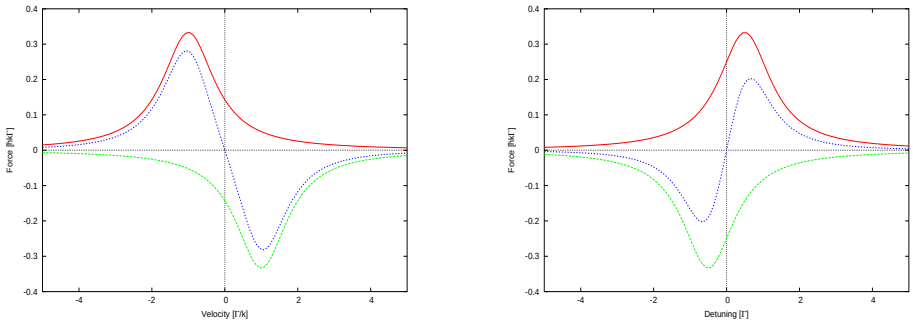

Figure 2.2: Optical damping force for a one–dimensional optical molasses as a function of a) the velocity b) the detuning. The red and green line are the individual forces originating from each laser beam and the blue line is the resulting total force.

2.4 The magneto–optical trap

As already mentioned, atoms in an optical molasses are cooled but not trapped. Applying, in addition to the light fields, an inhomogeneous magnetic field results in spatial confinement. An arrangement using laser light and magnetic fields in order to cool and trap atoms is called a magneto–optical trap (MOT). The first MOT in three dimension was demonstrated by Raab et al in 1987 [14]. The principle of a magneto–optical trap is shown in figure 2.3.

It consists of six counterpropagating laser beams and a magnetic field with a constant gradient being zero at the trap center. This quadrupole magnetic field is achieved by two magnetic coils in anti–Helmholtz configuration, meaning that the direction of the current in both coils is reversed. The magnetic field in the center is zero, increasing linearly in the positive x–direction and decreasing linearly in the negative x–direction. Because the magnetic field varies spatially, the atoms experience a position dependent scattering rate, which provides a force confining them to the zero of the magnetic field. In order to create this force, the laser beams must have an appropriate polarization. Figure 2.4 helps to explain the origin of this force in one dimension. In this simplified case the atom has a $J = 0$ ground state

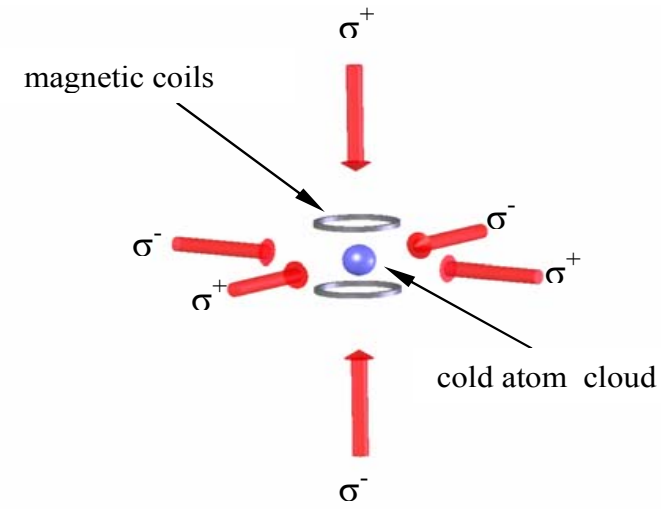

Figure 2.3: Schematic of laser cooling in a magnetic trap

and a $J = 1$ excited state (the scheme works for any $J_g \longrightarrow J_e = J_g + 1$ transition), illuminated by circularly polarized beams of light, coming from the left and the right. The light coming from the left is σ_+ polarized and therefore can only induce transitions with $\Delta m = +1$, whereas the σ_- light coming from the right can only induce transitions with $\Delta m = -1$. Because the magnetic field is inhomogeneous, the Zeeman splitting of the energy levels is dependent on the position of the atoms and increases with increasing distance from the center. In the center the energy levels are degenerate. An atom on the right hand side of the trap center, at position x' (see figure 2.4) absorbs only light coming from the right. This is because only σ_-–light can induce transitions to the $M_e = -1$ level; the $M_e = +1$ level is too far from resonance with the σ_+–light coming from the left ($\delta_+ > \delta_-$, see figure 2.4). As a result, all atoms which are on the right from the center (positive x), experience a force which pushes them to the left. Atoms which are left from the center (negative x) are pushed to the right, since here the situation is reversed and only σ_+ light is absorbed. A cold atom cloud is consequently created at the zero of the magnetic field. It is experimentally easy to extend this analysis to three dimensions, since the quadrupole magnetic field

is characterized by a constant gradient in all six room directions.

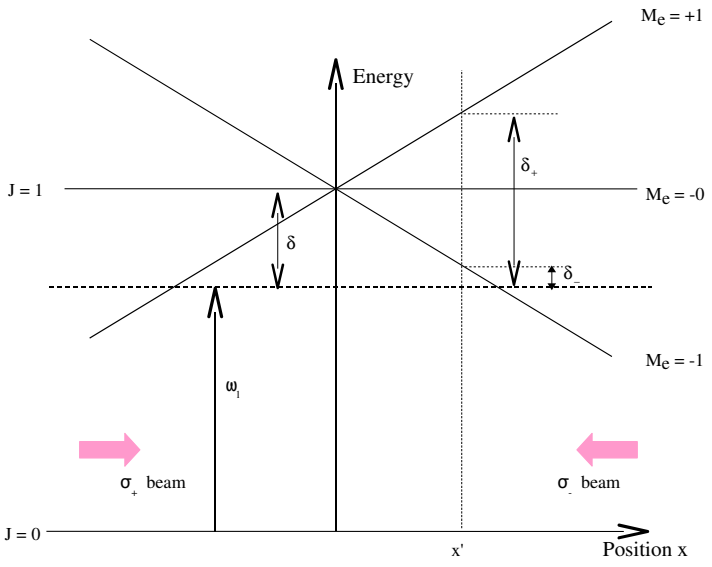

Figure 2.4: Origin of the position dependent force for a MOT in 1D. An atom at position x' only absorbs σ_- polarized light coming from the right and therefore is pushed towards the center.

The overall force acting on the atoms due to the velocity dependent scattering force and the position dependent force in 1D is given by:

$$F_{\mathrm{MOT}} = \frac{\hbar k \Gamma}{2} \left[\frac{I/I_0}{1 + 4\left(\frac{\delta - kv - \beta z}{\Gamma}\right)^2} - \frac{I/I_0}{1 + 4\left(\frac{\delta + kv + \beta z}{\Gamma}\right)^2} \right] \tag{2.4}$$

with $\beta z = \frac{g\mu_{\mathrm{B}}}{\hbar} \frac{\mathrm{d}B}{\mathrm{d}z} z$

where g is the g–factor of the atom and μ_{B} is the Bohr magneton. This expression can be rewritten for small velocities and small–Zeeman shifts:

$$F_{\mathrm{MOT}} = \frac{2\hbar k (2I/I_0)(2\delta/\Gamma)[kv + \beta z]}{[1 + (2\delta/\Gamma)^2]^2} \tag{2.5}$$

or

$$F_{\mathrm{MOT}} = -\alpha v - \frac{\alpha\beta}{k} z = -\alpha \dot{z} - Kz \tag{2.6}$$

Equ. (2.6) expresses the equation of motion of a damped harmonic oscillator with mass m, damping constant α, and spring constant $K = \frac{\alpha\beta}{k}$.

$$\ddot{z} + \frac{\alpha}{m}\dot{z} + \frac{K}{m}z = 0 \tag{2.7}$$

2.5 The Doppler–cooling limit

The damping force $F_{\mathrm{OM}} = -\alpha v$ [Equ. (2.1)] results in a loss of kinectic energy. The rate at which the atom looses kinetic energy is given by

$$\frac{dE_{\mathrm{cool}}}{dt} = \vec{F} \cdot \vec{v} = -\alpha v^2 \tag{2.8}$$

At the same time the atom is heated, since each absorption and emission process transfers a momentum of $\hbar k$ to the atom which changes its kinetic energy by the recoil energy $E_r = \hbar^2 k^2/2M = \hbar\omega_r$. The atom's momentum undergoes a random walk whose mean square, and therefore its kinetic energy increases with time. The light field loses an average energy of $2\hbar\omega_r$ for each scattering event at a rate of 2γ (since there are two beams) yielding a heating rate of $4\hbar\omega_r\gamma$ [13].

There is a temperature at which the rate of increase of kinetic energy due to diffusion is equal to the rate of decrease in kinetic energy due to damping and therefore a steady state is reached. It can be calculated by equating the cooling rate Fv [equ. (2.3)] with the heating rate $4\hbar\omega_r\gamma$ which leads to

$$v^2 = 4E_r\frac{\gamma}{\alpha}$$

Evaluating $\frac{\gamma}{\alpha}$ for the low intensity case (i.e. ignoring the term I/I_0 in the denominator of both α and γ) and employing the equipartition theorem ($\frac{1}{2}k_BT = \frac{1}{2}Mv^2$) yields

$$k_{\mathrm{B}}T = -\frac{\hbar\Gamma}{4}\left(\frac{\Gamma}{2\delta} + \frac{2\delta}{\Gamma}\right) \tag{2.9}$$

This expression is dependent on δ and it has a minimum at $\delta = -\Gamma/2$, giving the so called Doppler cooling limit T_{Dop}

$$k_{\mathrm{B}}T_{\mathrm{Dop}} = \frac{\hbar\Gamma}{2} \tag{2.10}$$

This is the lowest temperature which can be reached in the frame of a two–level atom. For ^{85}Rb it is 143.41 μK and for ^{6}Li it is 142.11 μK [13]

2.6 Sub–Doppler laser cooling

The derivation of the Doppler–cooling limit is rigorously based on a two level atom. The first failure of the two–level theory of optical molasses was discovered by the NIST group of W. Phillips in 1988 [17] when they found that sodium atoms could be cooled to temperatures much lower than the minimum temperature predicted by equ. (2.10), even approaching the recoil limit given by

$$k_{\mathrm{B}} T_{\mathrm{R}} = \frac{\hbar^2 k^2}{2M}$$

where M is the atomic mass. This is the kinetic energy of the atoms due to the last spontaneous emission event which leaves atoms with a residual momentum of the order on $\hbar k$. It is the lowest temperature which can be reached assuming the last photon scattering event is not selected or controlled in some way. Exotic cooling schemes have been discovered which allow one to even beat this recoil limit [18], [19].

Due to the inconsistency of the Doppler cooling theory and the experimental observations, a new model of laser cooling was required, that accounts for the fact that a two–level picture of atomic structure is not adequate. Two groups incolving C. Cohen–Tannoudji, J. Dalibard and S. Chu independently developed a theory of laser cooling that could explain the lower temperatures [15], [16] by including the multiplicity of atomic sublevels. This theory, however, goes beyond the frame of this thesis work. For more details, please refer to one of these references.

Chapter 3

Ultracold Molecules

The previous chapter dealt with the theory of cooling and trapping of neutral atoms whose experimental techniques got well established during the last 20 years. The extension to the molecular case, however, is not so easy. Laser cooling of molecules is a difficult problem due to the lack of a closed two–level scheme. Molecular states consist of many vibrational and rotational energy levels and therefore cannot be as easily cooled as neutral atoms. This chapter will give a short overview over the structure of diatomic molecules and, after explaining how ultracold molecules in general can be created by photoassociation, will present some theoretical investigations related to the photoassociation and detection of ultracold LiRb molecules.

3.1 Interaction Potentials

In this work we start with an ensemble of cold Rb and Li atoms. Then via a process known as photoassociation (description see below), individual Li and Rb atoms are associated together to form a diatomic molecule. In order to comprehend the photoassociation process, the interaction potentials at various inter–atomic distances must be understood. A molecule is held together by the shared electron cloud, the nuclei alone would repel each other. Two atoms approaching each other experience a force which is attractive at longer distances and gets repulsive at internuclear separations smaller than few atomic length units. Just as for atoms, there are different electronic states of the molecule, depending on the orbitals in which the electrons are. Each of these electronic states can be described by a potential curve. If

the molecule is stable, this curve has a minimum at a certain equilibrium distance, in the unstable case, there is no minimum because the atoms repel each other for any value of the internuclear distance. If the atoms are far apart, the interaction is dominated by the long–range Van–der–Waals force. At small distances the force between the atoms gets repulsive due to the overlap of electronic orbitals.

3.1.1 Short–range interaction

At small internuclear distances of some atomic units the wavefunctions of the electrons overlap and the electronic state can be described in terms of Hund's coupling case a). Its main characteristic is, that, in this region of the interaction potential, the coupling of the electron orbital momentum to the internuclear axis is stronger than the spin–orbit coupling. The electron orbital momentum of the electrons therefore add up to a total angular momentum $\vec{L}$ which rotates around the internuclear axis. A molecule described by Hund's case a) is shown in figure 3.1(a). The projection of $\vec{L}$ onto the internuclear axis gives the quantum number Λ. An electronic state described in terms of the Hund's coupling case a) is labeled in the following way:

$$^{2S+1}\Lambda^{\pm}_{\Lambda+\Sigma}$$

Λ can take the values $0, 1, 2, \ldots$ and, in analogy to the atomic case, these states are labeled by $\Sigma, \Pi, \Delta, \ldots$. S is the total electronic spin and its projection on the internuclear axis (which is only defined for $\Lambda \neq 0$) gives the quantum number Σ which can take values from $-S, -S+1, \ldots, S-1, S$. The $\pm$ indicates the symmetry according to any reflection which contains the internuclear axis. Furthermore, the molecule can rotate around an axis perpendicular to the internuclear axis which results in an additional angular momentum (not shown in figure 3.1(a)).

The short–range potential curves can be modeled by a Morse potential which has the form

$$V_{\text{Morse}} = D_e \left[\left[1 - \exp\left(-\beta(R - R_e)^2\right) \right]^2 - 1 \right] \tag{3.1}$$

where D_e is the dissociation energy, R the internuclear distance, R_e the equilibrium internuclear distance and $\beta = \sqrt{\frac{\mu}{2D_e}}\omega_e$, where μ is the reduced mass and ω_e the vibrational frequency of the molecule.

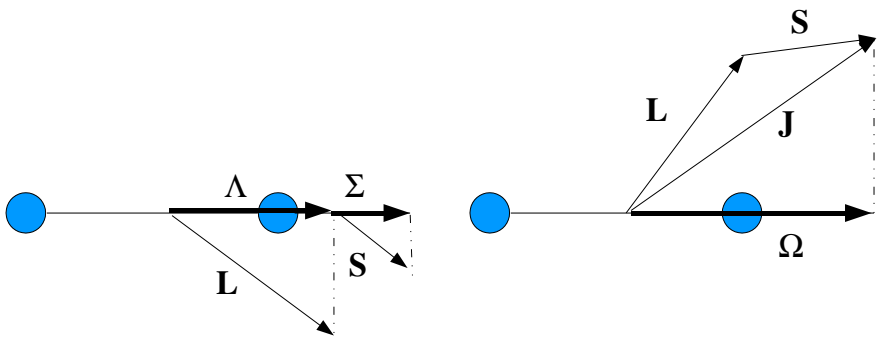

(a) (b)

Figure 3.1: A molecule described by a) Hund's coupling case a); b) Hund's coupling case c)

3.1.2 Long–range interaction

At large interatomic distances, a molecule is described by Hund's coupling case c). The spin–orbit interaction is stronger than the coupling of the orbital momentum to the internuclear axis. The total orbital momentum $\vec{L}$ and the total spin momentum $\vec{S}$ of the electrons couple to a total angular momentum $\vec{J}$. Λ and Σ are no good quantum numbers anymore, and the molecular state is labeled in the following way:

$$\Omega^{\pm}_{u/g}$$

where Ω is the quantum number of the projection of the total angular momentum $\vec{J}$ on the internuclear axis (see figure 3.1(b)). The $\pm$ and u/g indicate the reflection symmetry in an arbitrary plane containing the internuclear axis, the parity (*ungerade*, meaning odd and *gerade* even), respectively.
Hund's coupling case c) is valid for internuclear distances approximately larger than 20 a_0, where a_0 is the Bohr radius. At these distances the interaction is governed by the Van–der–Waals force and the potential can be expanded in the following series:

$$V_{\text{Longrange}} = D_e - \sum_n \frac{C_n}{R^n} \tag{3.2}$$

where D_e is the dissociation energy and R the internuclear distance.

The coefficients C_n correspond to the different electric multipoles [21] and can be calculated with the help of perturbation theory. C_1, C_2 and C_4 all are only non–zero if one of the atoms is an ion. The odd coefficients represent dipole–dipole interactions (C_3), quadrupole–quadrupole interactions (C_5) and so forth between the colliding atoms and vanish for atoms in the ground state, since they do not have permanent electric moments. For a homogeneous molecule, however, the C_3 coefficient is nonzero if one atom is in the excited state as can be shown with perturbation theory [22]. The even coefficients originate from induced dipole–dipole interactions (C_6), induced dipole–quadrupole interactions (C_8) and so forth and are the only non–zero coefficients for a heteronuclear molecule. Therefore, the long–range potential of a diatomic, heteronuclear molecule can be approximated by

$$V_{\text{Longrange}}(R) = D_e - \frac{C_6}{R^6} - \frac{C_8}{R^8} - \frac{C_{10}}{R^{10}} \tag{3.3}$$

The intermediate part of the potentials can be neither described only by the Hunds case a) or c). In fact, Hunds case c) potentials are mixtures of Hunds case a) potentials as described in [20].

3.2 Formation of Ultracold Molecules – Photoassociation

Cooling molecules is much more difficult than cooling atoms and cannot be achieved by laser cooling techniques. Therefore, during the last years, a variety of methods to create cold molecules has been developed. These methods can be divided into two groups: “direct” methods, based on cooling pre–existent molecules and “indirect” methods where molecules are formed from pre–cooled atoms [23]. Direct methods, such as buffer–gas cooling [24] or Stark–deceleration [25] start with relatively hot molecules and do not result immediately in as low translational temperatures as the indirect methods, where translational temperatures in the microKelvin region can be obtained. The indirect methods of photoassociation and Feshbach resonances start with first cooling the constituent atoms and then making molecules resulting in translational temperatures as cold as in the atomic sample. The following section will give a brief introduction to photoassociation, since this is the technique which will be used in our experiment in the near future. For more

details, please see these two excellent review articles [26], [27]. Our experiment will also allow to study cold molecules created via Feshbach resonances. Detailed information on Feshbach resonances can be found in [29].

Photoassociation was first proposed in 1987 by Thorsheim et al. [28]. The principle is the following: Laser cooled atoms collide in their electronic ground state at almost zero kinetic energy. If during the collision they absorb a photon of suitable frequency ω_{PA}, the ground state atom pair can be excited into a molecular bound state. This process is illustrated in figure 3.2.

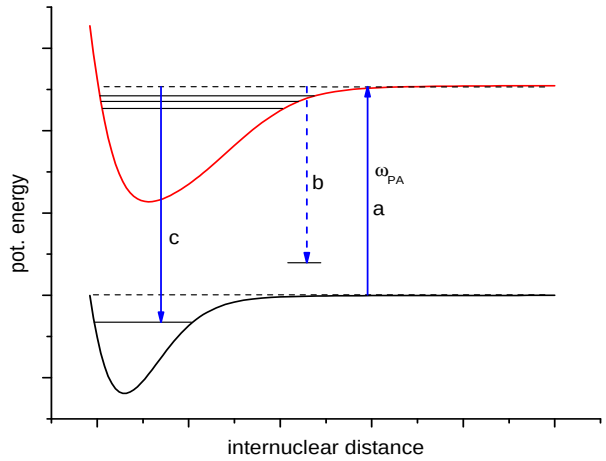

Figure 3.2: Photoassociation of ultracold molecules. a) A colliding pair of atoms absorbs a photon and is excited to a bound molecular state; b) The molecule decays either to two free atoms or c) to a bound ground state molecule that as shown is vibrationally hot.

Suitable frequency means here, that the energy of the photon must correspond to the energy difference between the ground state level and a vibrational level of the electronically excited molecular state, i.e

$$\hbar\omega_{\mathrm{PA}} = E_i^{(e)} - E_{tot}^{(g)} \tag{3.4}$$

where $\hbar\omega_{\mathrm{PA}}$ is the energy of the photon, $E_{tot}^{(g)}$ is the total energy of the colliding ground state atoms and $E_i^{(e)}$ the total energy of the ith bound excited state. The created molecules are – neglecting the recoil energy – translation-

ally as cold as the atomic sample. A drawback is, that the molecules are formed in a rotational and vibrational level of the electronic excited state and decay very quickly by spontaneous emission. In most cases, they spontaneously decay to two free atoms (see arrow b) in figure 3.2). The photon energy of the emitted photon in almost all cases is red detuned with respect to the photon which photoassociated the molecule. The remaining energy converts into kinetic energy of the free atoms, which are too hot to remain in the trap. The excited molecule can also decay to a bound ground state (see arrow c) in figure 3.2), however, the probability for this event to happen is very low. The ground state molecules will leave the trap as well. Photoassociation events therefore can be observed as a trap loss. Scanning the frequency w_{PA} of the photoassociation laser results in a fluorescence spectra characterized by a series of dips, since as ω_{PA} passes through a free–bound resonance, the number of atoms and therefore the intensity of the fluorescence in the trap reduces. The resolution is limited by the width of the statistical distribution of the initial kinetic energy of the colliding atoms, which is of the order of $k_{\mathrm{B}}T$. At ordinary temperatures, these spectra are very broad, but at temperatures of around $100\,\mu$K (which corresponds to approximately 2 MHz) very high resolution is achieved. Since the probability of finding two atoms at a distance R scales with R^2, photoassociation is efficient mainly at large interatomic distances and is therefore particularly suitable to study the long–range molecular states. This has consequences for heteronuclear dimers. Since the excited state potential of a heteronuclear dimer varies as R^{-6} in contrast to homonuclear dimers where it scales with R^{-3}, the photoassociation rate is predicted to be lower for heteronuclear dimers.

3.3 Towards cold LiRb–molecules

The immediate goal of this experiment is the creation of cold LiRb–molecules from a dual–species MOT and their observation and detection via a trap–loss spectrum. The first step is to cool simultaneously Li and Rb in a MOT, then to create LiRb molecules by scanning the photoassociation laser and record the fluorescence. In order to be able to interprete this spectrum, some theoretical knowledge about the LiRb molecule, especially its potential curves is helpful. After describing first the cooling process of Li and Rb in a MOT, this chapter will present some theoretical investigations and literature related to the LiRb molecule.

3.3.1 Cooling of Li and Rb in a MOT

The first step towards cold LiRb–molecules is laser cooling and trapping of both Lithium (^{6}Li) and Rubidium (^{85}Rb and ^{87}Rb) atoms in a dual–species MOT. Figure 3.3 shows the energy levels and the relevant transitions for ^{6}Li.

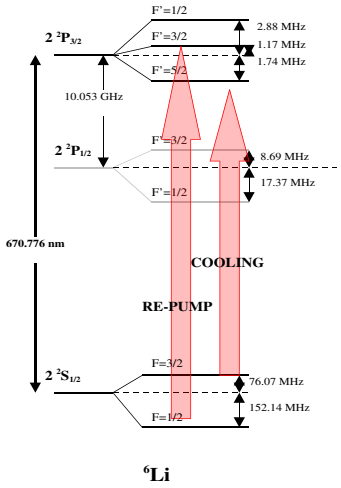

Figure 3.3: Schematic of lithium energy level diagram with the laser cooling and repump light shown for ^{6}Li. (taken from [30])

The ground state of ^{6}Li is split into two hyperfine states, which requires besides the cooling laser ($F = 3/2$ to the $2P_{3/2}$–manifold) a repump laser ($F = 1/2$ to the $2P_{3/2}$–manifold) in order to avoid optical pumping to the $F = 1/2$ ground state level. The hyperfine splitting for ^{6}Li is small (228 MHz for the ground state) because of its small mass. For the excited state (4.6 MHz) it is even smaller than the natural linewidth of the transition (6 MHz), such that it can considered as one single energy level, since all spectral features due to the hyperfine splitting are washed out. Li therefore can be treated as a three–level system with two ground– and one excited state. However, due to the small hyperfine splitting, the optical pumping process is very strong, since atoms are easily excited to the $F' = 3/2$ hyperfine level from where they can decay to the dark $F = 3/2$ ground state level, what requires a repump beam with is similar in power than the cooling beam. Since the number of scattered repump atoms is comparable with the number of cooling

transition photons, we send it in from all six room directions, ensuring that the radiation pressure from scattering the repump is symmetric.
The energy levels and involved transitions for ^{85}Rb and ^{87}Rb are shown in figure 3.4. Unlike Li, the hyperfine splitting of the excited state is large, such that the probability for an atom to be pumped to the $F = 1$ for ^{87}Rb, $F = 2$ for ^{85}Rb state, respectively, is much lower than for Li.

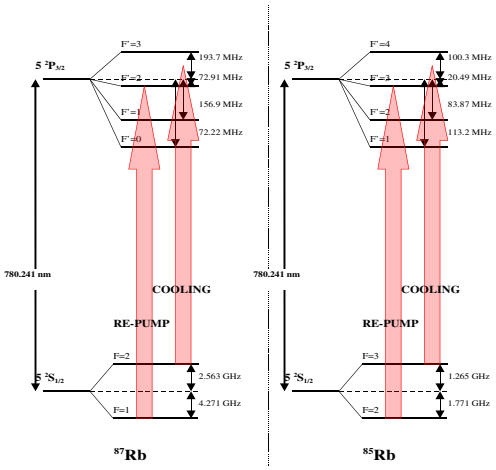

Figure 3.4: Schematic of the rubidium energy level diagram with laser cooling and repump light shown for ^{85}Rb and ^{87}Rb. (taken from [30])

3.3.2 Properties of LiRb

To the best of my knowledge, no experimental data are yet available for the potentials and energy states of the LiRb–molecule. However, some quantum chemical calculations have been performed on this molecule. Its ground state among the other nine alkali dimers was investigated in [31]. Results from these calculations for the bond length, dissociation energy, vibrational frequency, dipole moment and ionization energy are summarized in table 3.1.

Interesting is here the large permanent dipole moment of 4.13 D, which is only exceeded by the dimers LiCs and NaCs (table V of [31]) and makes the LiRb–molecule a promising candidate for experiments involving electric field manipulations.

Bond length R_e	3.45 Å
Dissociation energy D_e	0.73 eV
Vibrational frequency ω_e	195 cm^{-1}
Dipole moment d	4.13 D
Ionization energy IP	4.38 eV

Table 3.1: Ground state properties of the LiRb molecule (data taken from [31])

.

Data for the molecular potentials for the first 28 lowest states up to the dissociation limits Li(2s) + Rb(5d) are calculated in [32]. However, these calculations are performed in the Hund's coupling case a) ignoring the spin–orbit coupling. Due to this approximation these calculations are not very accurate in the long range case (the $2s+5p$–asymptote lies at 785 nm instead being split into a D1 and a D2 line at 780 nm, 795 nm respectively). However, it was still very helpful to get a first impression of the potential curves and for choosing a suitable ionization laser as described in the last section of this chapter. This data for the ground and the first excited state is shown in figure 3.5. There are two states belonging to the ground state asymptote 2s + 5s, a triplet ($^3\Sigma$) and a singlet state ($^1\Sigma$), whereas the excited state (2s + 5p) consists of four states ($^1\Sigma$, $^3\Sigma$, $^1\Pi$, $^3\Pi$).

This data does not take the fine structure into account. However, for photoassociation experiments, the long–range states are of particular interest. Results on the longe–range potential curves, i.e. the C_6 and C_8–coefficients [equ. (3.3)] are reported in [33]. These potential curves using the C_6^* and the C_8^* constants presented in table IX and X of Ref. [33] are plotted in figure 3.6 for the four lowest asymptotes:

$$\mathrm{Li}(2s)+\mathrm{Rb}(5p_{1/2}),\ \mathrm{Li}(2s)+\mathrm{Rb}(5p_{3/2}),\ \mathrm{Li}(2p_{1/2})+\mathrm{Rb}(5s),\ \mathrm{Li}(2p_{3/2})+\mathrm{Rb}(5s)$$

Since the energy separation between the Li D1 and D2 line is so small, it is drawn just as one single $2p + 5s$ asymptote in figure 3.6.

One striking feature is, that of the four excited asymptotes only the two lower ones generate attractive states, whereas the two higher ones with Li in the excited and Rb in the ground state form only repulsive states.

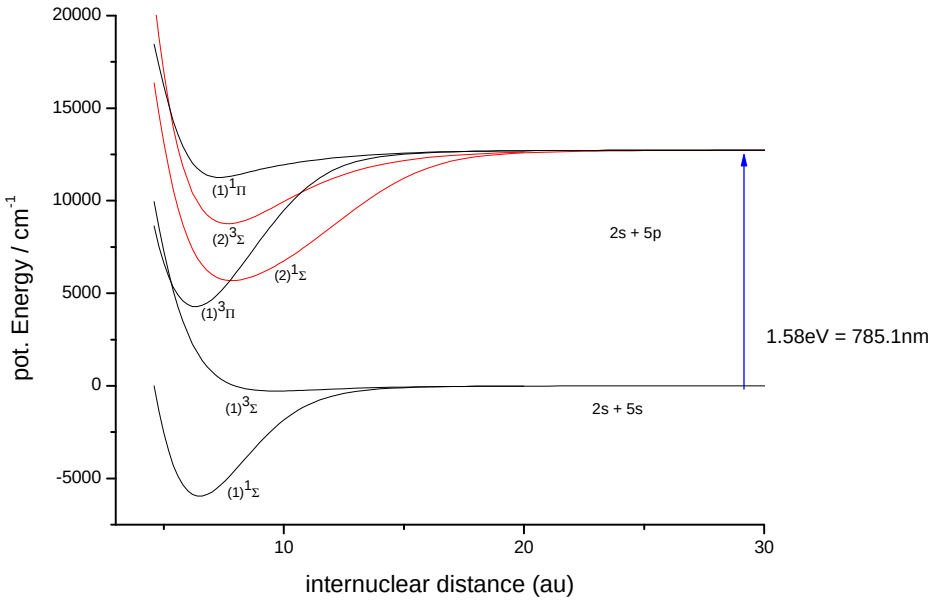

Figure 3.5: Potential curves for the ground and first excited state of LiRb (data from [32]).

3.3.3 Photoassociating Li and Rb

Three different molecules will be produced simulataneously in the dual–species MOT: ^{6}Li^{85}Rb (or ^{6}Li^{87}Rb) by using a Ti:Sapphire Laser as photoassociation laser. In addition, automatically, $^6Li_2$ and $^{85}Rb_2$ (or $^{87}Rb_2$) will be formed because the MOT light is red detuned and therefore by virtue can excite the atoms to some highly excited vibrational levels close to the atomic asymptote. The frequency of the photoassociation laser will be scanned from 780 nm which corresponds to the $2s + 5p_{1/2}$ asymptote down to the red. We expect to see a series of dips in the spectrum belonging to different vibrational levels of the long–range states. From these specta, information on the energy levels of the excited state and the shape of the excited state potential curve can be obtained. In addition, since we are equipped with two Ti:Sapphire lasers, we can perform a two–color experiment driving the excited molecules to the ground state mapping out the ground state energy levels and potential

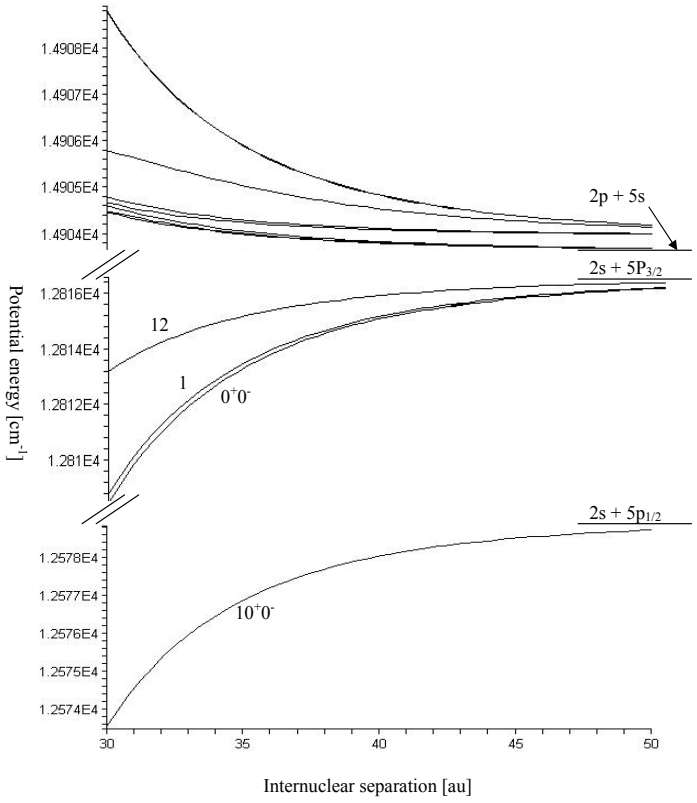

Figure 3.6: Long–range potential curves for the first excited state of the LiRb molecule (data taken from [33])

curve shapes.

3.3.4 Creation of LiRb ions

Detecting the molecules by recording the trap loss does not allow to distinguish between excited molecules decaying to two atoms leaving the trap or a molecule decaying to a bound ground state level. Furthermore, it is not possible to distinguish between the different kinds of molecules. A very efficient method to detect single molecules is time–of–flight mass spectrometry. Instead of detecting the neutral molecules, the molecules are ionized and accelerated by an electric field onto a micro–channel plate detector. This

method allows to distinguish between molecules of different masses. Positive ions are created by photoionization with a pulsed laser of suitable frequency. The most suitable and convenient laser source would be a tunable laser at around 600 nm, but we chose a Q–switched frequency doubled Nd:YAG laser emiiting at 532 nm which was already available in the lab. The reasons for this choice will be explained with the help of the following figure 3.7, which shows some relevant energies related to the ionization of LiRb molecule.

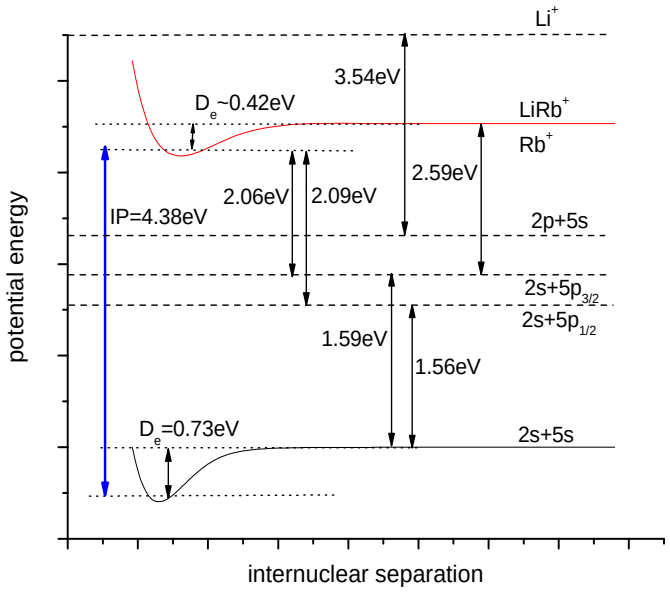

Figure 3.7: Relevant energies related to the ionization of LiRb

A 532 nm photon (2.33 eV) is sufficient to excite the LiRb–molecules from the $2s + 5p_{1/2}$ as well as the $2s + 5p_{3/2}$ asymptote to a bound state of the molecular ion, but is too low to dissociate the molecular ion in a one–photon process, since the dissociation energy of the molecular ion is too large (0.42 eV taken from [34]). This wavelength was chosen also because the ionization of Li and Rb atoms from their ground or first excited state requires two photons and is therefore suppressed. This is favorable, since we are interested in the molecular signal only. 2.33 eV is much too little energy to ionize Li or Rb from their ground state in a one–photon process and having a look at the

atomic energy levels tells that a two–photon REMPI process (resonanced–enhanced multiphoton ionization) is impossible, since there are no matching energy levels. In addition, neither Rb nor Li atoms can be ionized in a one–photon process from their first excited state (see figure 3.7). The next possible ionization process is a two–photon non–resonance enhanced. The probability for this to happen is small compared to a one–photon or a two–photon REMPI process. All this should keep the signal coming from Li^+ and Rb^+ ions weak. It would be more convenient to have a tunable laser source at around 600 nm, but since we had the 532 nm Nd:YAG available in the lab

Chapter 4

Experimental Setup

For this thesis work, along with other students, I constructed an operational dual species Li and Rb MOT. This chapter describes the experimental setup as it has been built from the ground up during the last year. This includes the construction and the bake–out of the vacuum system, the atomic sources for Rb and Li, the laser system for the MOT as well as for the photoassociation experiment, the magnetic coils and the design and construction of a time–of–flight mass ion spectrometer. Figure 4.1 shows a three–dimensional drawing of the set–up, while figure 4.2(a) and 4.2(b) show two corresponding photographs of the experiment including the optical table.

.

4.1 Vacuum system

The most important part of the vacuum system is the trapping cell, which is completely made of glass in order to allow good optical access for the laser light. It was purchased from OptoSigma and is made of optical quality (highly polished) Borosilicate glass. It is 9.5 cm long, has an inner diameter of 20 mm and an outer diameter of 30 mm and is connected on both sides to the rest of the vacuum system by glass–to–metal seals purchased from MDC and Larson Electronics. The welding of the square cell on the glass–to–metal seals was done by Ron Bihler at Technical Glass. On one of the ends an electrical feedthrough is attached which holds the Li and Rb sources, the other one extends to a four way cross holding the micro–channel plate (MCP) detector and two vacuum pumps, an ion pump and a non–evaporable

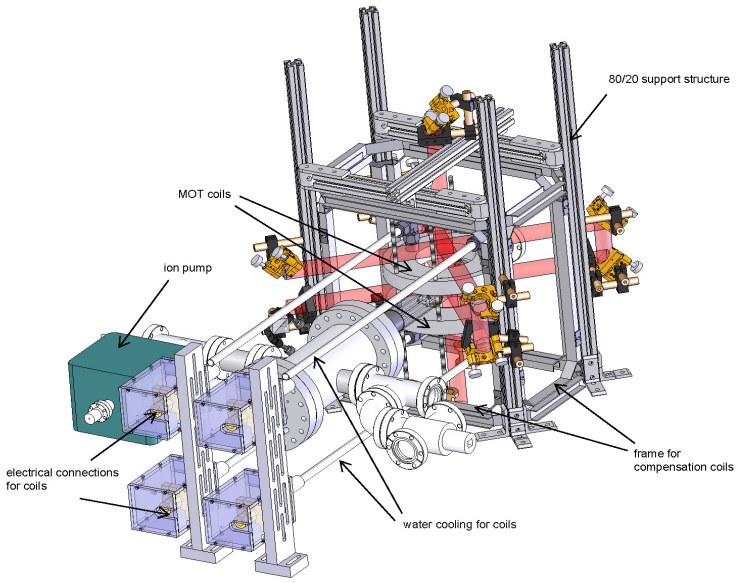

Figure 4.1: 3d drawing of the experimental setup.

getter (NEG) pump. Figure 4.3 gives a two dimensional view of the vacuum chamber showing the basic layout.

.

The primary concern in the construction of the vacuum system is that a ultrahigh vacuum (UHV) is required. In order to reach trap lifetimes long enough for most experiments of interest, pressures in the range of about 10^{-8} torr to 10^{-10} torr are required. Two vacuum pumps and a careful cleaning and bake–out procedure made it possible to reach a pressure of about 10^{-9} torr.

4.1.1 Vacuum pumps

Three vacuum pumps were involved in the construction of the vacuum system: A turbo molecular pump (Varian V70, pump speed 70 l/s), an ionpump (Varian StarCell, 20 l/s) and a non–evaporable–getter (NEG) pump (SAES CapaciTorr, > 100 l/s for H, H_2O). We used the turbopump during the bake out when large pumping speeds were required in order to drive out all the degassing materials. A turbopump creates a vacuum with the help of a rapidly spinning turbine rotor which “hits” gas molecules from the inlet of the pump

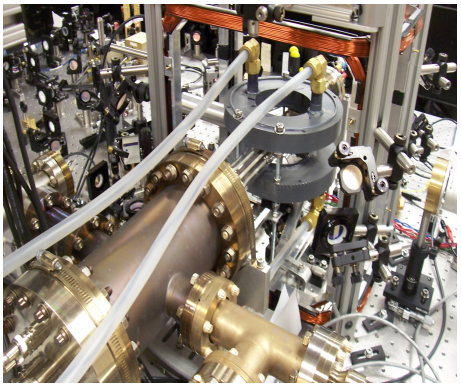

(a)

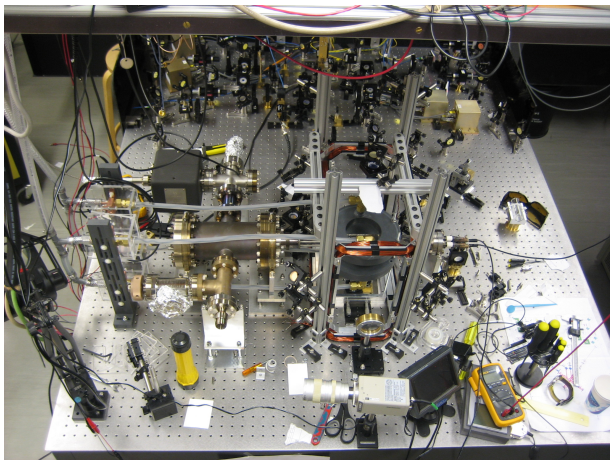

(b)

Figure 4.2: Two photographs of the experimental setup

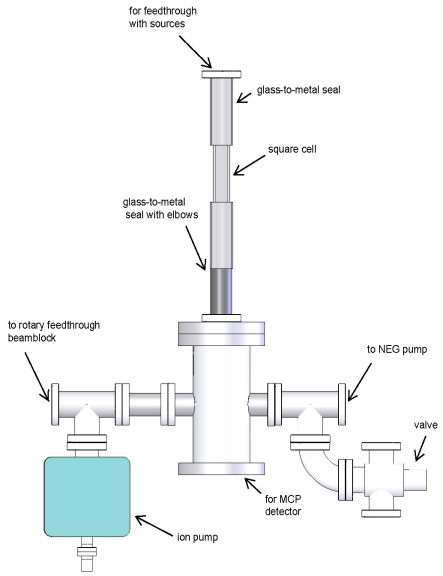

Figure 4.3: 2d view of the vacuum system showing the basic layout.

towards the exhaust.

The ion pump and the NEG pump are permanently attached to the vacuum system. An ion pump works by ionizing the residual gases in the vacuum by collisions with electrons so that they can be adsorbed to reactive metal (such as Titanium) on the walls of the pump. This ion burial is the basic means of pumping noble gases out of the chamber. The disadvantage of ion pumps are that they contain a strong permanent magnet in order to cause the ionizing electrons to spiral and, in spite of shielding, producing a stray magnetic field in regions close to the pump. Therefore, we put the ion pump as far as possible from the trap cell as well as from the time–of–flight mass ion spectrometer to avoid any disturbtion of the ion trajectories.

In addition to the ion pump, a NEG pump is connected to the chamber. A NEG pump contains a highly reactive getter material which is activated by heating the material up by sending a current through it. For the SAES CapaciTorr a mixture of two getter materials is used, one is a Ti-V alloy (ST185), the other one a sintered Zr-V-Fe alloy (ST172). The heating causes the passive layer to diffuse into the bulk of the getter material and the residual gases in the vacuum are adsorbed to the surface by chemical reactions. A NEG pumps hydrogen and water very efficiently.

4.1.2 Cleaning and bake–out

Cleaning procedure

The cleaning procedure of the vacuum components proceeded as follows:

- 30 min in the ultrasonic cleaner with hot water and a detergent (alconox)
- 15 min (once or twice) rinsing in distilled water in the ultrasonic cleaner
- 15 min (once or twice) in the ultrasonic cleaner with methanol
- 15 min (once or twice) in the ultrasonic cleaner with acetone
- Dry in air and wrap in clean aluminum foil until needed for use.

Any surface which was to be used at high vacuum was never touched directly after it had been cleaned in order to avoid stray fingerprints occuring in the chamber. Rather all handling was done with latex gloves.

Air bake–out

After the cleaning all stainless steal vacuum parts (no valves) and all mounting components were airbaked in a home built oven up to $400 - 450\,^{\circ}\mathrm{C}$ for 3–4 days in order to burn off any residual contamination left on the parts.

Assemble and leak check

After the air bake–out the parts were carefully assembled using new, clean copper gaskets when making the conflat–type seals, as well as silver–plated bolts, and tightening down the flanges uniformly. The vacuum system was attached to the turbo pump station, which also contained a residual gas analyzer (SRS–200 RGA), and pumped down. We checked all seals for leaks by directing a helium source around them, with the help of the RGA, watching for any sign of helium being sucked into the chamber. We found some parts leaking, probably due to the fact that we accidently performed the air bake at too high of a temperature. These components were replaced by non–air baked spare parts.

Preliminary bake–out

Since all the vacuum parts were exposed to the humid air typically present in Vancouver, the components of the surrounding air (mainly water vapour) become adsorbed to their surface. These components slowly outgas keeping the pressure high inside the chamber. In order to reduce this source of contamination, the vacuum system is heated up while being pumped such that the absorbed components evaporate, leave the surface and are pumped out. We did the bake–out in two steps. For the preliminary bake–out the system was baked at 200 °C for a few (5–10) days. At this point, the system already included the atomic sources and the ion pump, but not yet the glass cell and the MCP. We flashed the ion pump several times and finally turned it on before the pressure went too low. The temperature was not changed faster than 1 °C/min in order to avoid thermal stress. Each rise in temperature is accompanied by a rise in pressure (since the adsorbed components leave the surface) followed by a slow drop (since they are pumped out), as seen in figure 4.4 which shows the pressure during our preliminary bake out as a function of time.

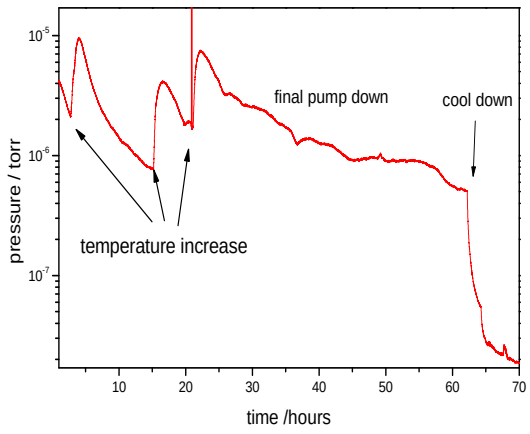

Figure 4.4: The pressure in the chamber during the preliminary bake–out as function of time. Each increase in temperature causes an increase in pressure followed by a pump down.

Final bake–out

The entire system, now including the ion pump as well as the NEG pump, the glass cell and the time–of–flight spectrometer was baked at around 200 °C for more than one weak. Thermocouples were used to track the temperature in the oven making sure that the temperature did not exceed 200 °C. At this point we also activated the NEG pump. Figure 4.5 shows the vacuum system in the home built oven short before the final bake out. Note the different coloration of some of the components. The dark purple looking parts were air baked, the silver components are non–air baked spare parts which we used to replace some of the leaking air baked parts. The oven is built from pottery bricks wrapped in aluminum foil and is heated up with five ceramic heaters.

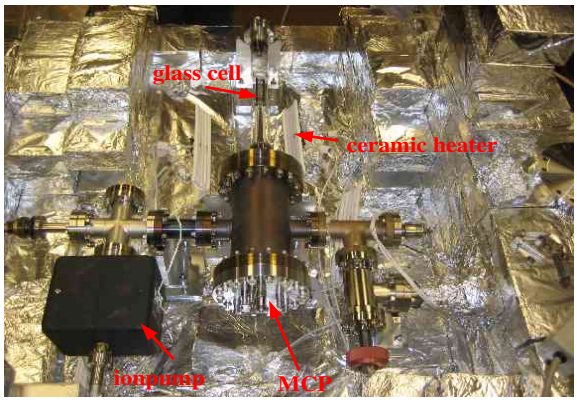

Figure 4.5: The vacuum chamber ready for the final bake out.

4.2 Atomic sources

4.2.1 Rubidium source

For Rb we use a commercial dispenser (SAES Getters) which releases ^{85}Rb and ^{87}Rb in their natural abundances of 72.17 % and 27.83 % when the getters are resistively heated with a few amps of current. The dispenser contains

a Rb compound (Rb_2CrO_4) and a reducing agent (ZrAl) enclosed in a stainless steel container having a trapezoidal crosssection. When current is passed through it, its temperature rises to several hundred $°C$. At these high temperatures, the Rb compound undergoes a reduction reaction and atomic Rb is released through a slit [35]. Dispensers are convenient, since they are inexpensive and easy to handle inside UHV systems. Being placed close to the trap center, the supply of atoms can be switched off quickly by turning down the heating current [35]. In our experiment it is rather far away from the trap center (14 cm) and is operated continuously. We use the source as a thermal source and load atoms from the slow atom tail of the hot background vapor. We have installed two dispensers by drilling holes through the copper rods of a UHV feedthrough and sliding the leads of the dispenser through them, bending them in order to hold them tightly. We were careful to mount the dispenser such that the thermal dispenser–copper contact area is the same on both sides of the dispenser, since we want it to heat up homogeneously. Figure 4.6 shows the feedthrough from the top with the two dispensers and the Li oven (see next section).

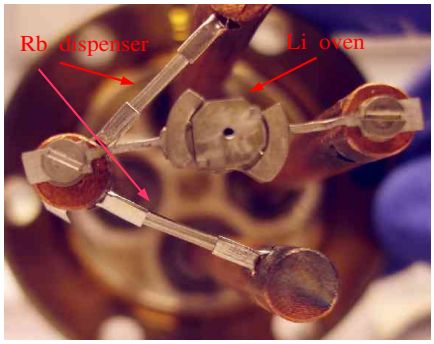

Figure 4.6: The UHV feedthrough from the top with the two Rb dispensers and the Li oven.

Since we knew from previous tests, that the dispenser emits other gases besides Rb, mainly hydrogen, nitrogen and all other components of the air, we outgassed the dispenser before putting it into the vacuum chamber for the bake out in order to avoid contamination when turning it on the first time. The feedthrough containing two dispensers was therefore mounted on the turbo pump station, and with the help of the RGA the outgassing

behaviour while changing the current running through the dispenser was studied. Figure 4.7 shows a typical plot of the partial pressure of several gases as a function of time. Each spike in pressure is due to a rise of the heating current.

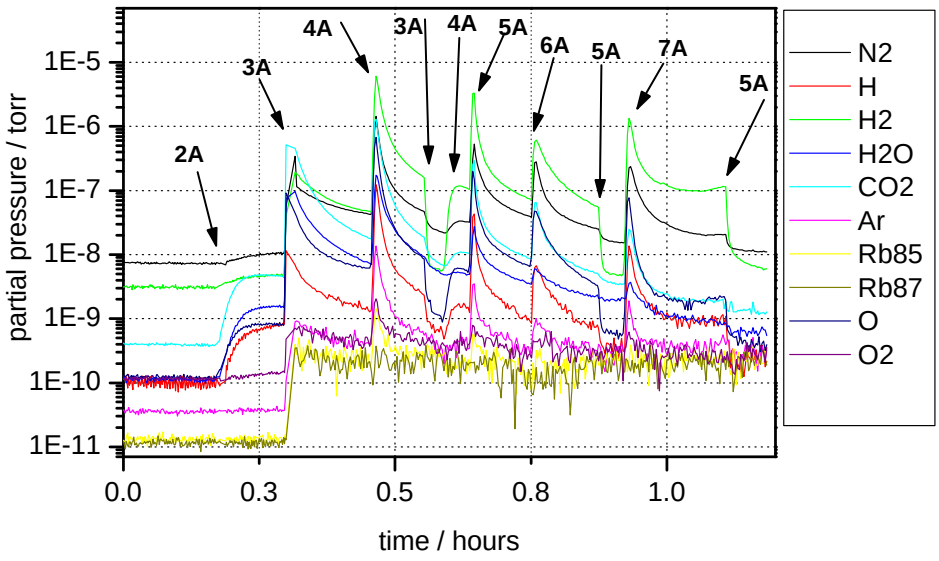

Figure 4.7: Study of the outgassing behaviour of the Rb dispenser with changing current. Plotted is the partial pressures of some common gases as a function of time. Each peak in pressure corresponds to an increase of current.

The outgassing process started at a current of 2 A. At a current of 3 A, the pressure went up so high that we had to switch off the electron–multiplier of the RGA in order to avoid damage. This explains the cut–off of the peaks and the increase of the background level. This sudden raise is due to the gases which stuck to the surface and were all at once released as soon as the dispenser heated up a bit. At 4 A the pressure level increased even higher to a value close to 10^{-5} torr. From then on, even at higher currents, up to 7 A, the pressure did not go up as high as before, indicating that most of the gases adsorbed to the surface are driven out. At the end, at a current of 5 A, the pressure would still be below 10^{-8} torr which is sufficient for our purposes.

Even though the dispenser will be reexposed to air after the outgassing, it would not absorb as much gas as it did initially. This we know from a previous test, when studied the outgassing behaviour of a dispenser before and after exposing it to air for one hour.

4.2.2 Lithium source

As for Rb, there are two isotopes for Li: the fermionic ^{6}Li and the bosonic ^{7}Li with natural abundances of 7.5 % and 92.5 %. We are interested in trapping the fermionic isotope, because the resulting molecules will be fermionic (since both ^{85}Rb and ^{87}Rb are bosones) and can be therefore stored and studied in an optical lattice as suggested in [36], [37]. Since there are no commercial dispensers available for ^{6}Li, a tiny oven made of NiCr consisting of a reservoir with a volume of approximately 80 mm^3 containing a small piece of a ^{6}Li enriched crystal and a lid with an exit hole was designed. Running a current of 10 to 11 A through it, the Li evaporates and the oven acts as an collimated atomic beam source. Similarly to the Rb dipsenser, we tested the oven mounted on the same feedthrough attached to the turbopump station. A laser beam, which had a frequency corresponding to the ground–excited state transition of Li, was sent into the chamber through a glass window and passed right above the exit hole. Fluorescence light in this beam would indicate any released Li. At a current of 9 A we saw the first sign of fluorescence, however, at a current of 10 A all the Li was suddenly released at once resulting in a huge burst of fluorescence along all the part of the beam inside the chamber. Melted Li apparently did not leave the reservoir only through the exit hole but also through the crack between the lid and the reservoir body. This problem was solved by putting a tiny stainless steal mesh into the reservoir which should keep the melted Li at the bottom of the reservoir and reloading it only half way with Li. Subsequent testing at currents up to 12 A indicated that the mesh had done its job and the fluorescence of the beam indicated that Li was released only through the exit hole and seemed to be well collimated. As for the Rb dispenser, we wanted to be sure that running the oven for the first time would not contaminate the chamber. Therefore, we studied the outgassing behaviour in the same manner as we did for the dispenser: Increasing the current in steps and recording the RGA signal for some common gases. Figure 4.8 shows the result.

Similar to the dispenser, mainly hydrogen is released and the pressure at the end (9 A) does not go up as high as at the beginning (5 A), a sign that

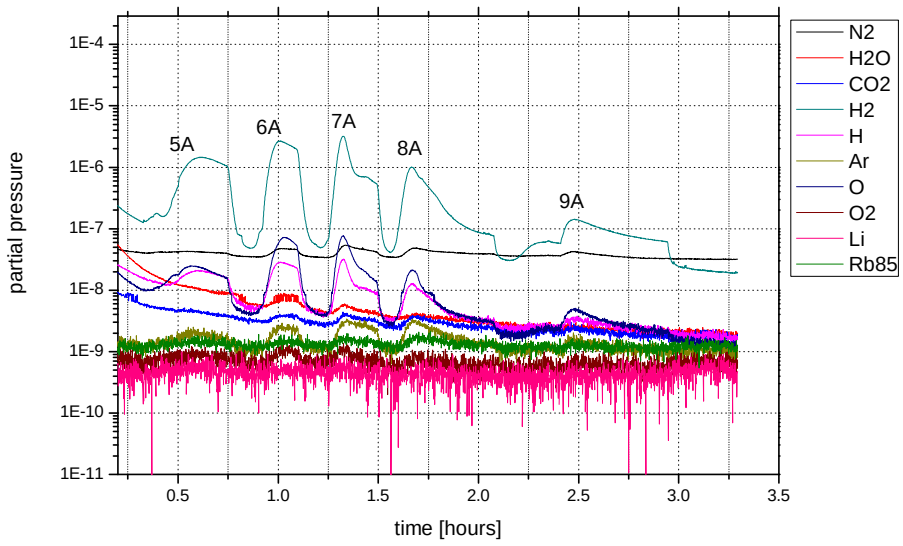

Figure 4.8: Study of the outgassing behaviour of the Li oven.

the outgassing procedure was succesful. This plot shows only currents up to 9 A, however, we tested the oven up to a current of 12.5 A and we were able to run it at this current at a pressure lower than 10^{-8} torr

4.3 The laser light

Several different types of lasers are used in the experiment. Semiconductor lasers are used to produce the cooling and repump light, an Argon–ion pumped Ti:Sapphire laser locked to a fiber comb for the photoassociation light, a fiber laser as the optical tweezer and a pulsed Nd:YAG laser for the photoionization.

4.3.1 Cooling light

Since we want to cool both Li and Rb, we need cooling light of different wavelengths, namely 780 nm for Rb and 671 nm for Li. Both of these must be red–detuned to the atomic transition and it is necessary to be able to change the detuning since the number of trapped atoms depends strongly on the detuning. In order to trap as many atoms as possible, a high optical power is favorable and the frequency must be stable. As explained in chapter 1, besides the cooling light a repump light for each species is also required. In MOT experiments, usually semiconductor lasers are used. This section will give a brief overview of how the cooling light is generated. For more details please refer to [30] or [39].

The master table

In a semiconductor laser, similar to light–emitting diodes (LEDs), the active material is a diode formed from a p–n–junction and radiation is emitted by recombination of holes and electrons when applying a forward bias (by sending some "injection current" through the diode). The wavelength of the emitted photons is determined by the band gap of the semiconductor. In our set–up we use different kinds of laser diodes for the Li and the Rb light with a band gap sufficiently close to the corresponding atomic transition.

The output of a single laser diode being too weak to share between separately running experiments and the diagnostics and desiring the cooling light to have as high power as possible, the light has to be amplified. The light is generated by so called master lasers, which generate ultra–stable well–collimated light by an external cavity. Frequency selective feedback obtained by a grating in Littrow arrangement provides the user with tunability and narrow bandwidth. The master light can be locked to a certain atomic transition by saturated absorption spectroscopy sending a fraction through a Rb absorption cell or a Li heat pipe. Amplification is obtained by injecting several "slave lasers" with the master light. A slave laser is another diode laser and being optically injected by the master light, it is forced to run single–mode at the same frequency as the master light. This serves to amplify the master light because the output power of the slave ($20 - 40\,\mathrm{mW}$) is greater than the amount of injection light used ($0.7 - 2\,\mathrm{mW}$)

In total, there are five master lasers. One master generates the Li light.

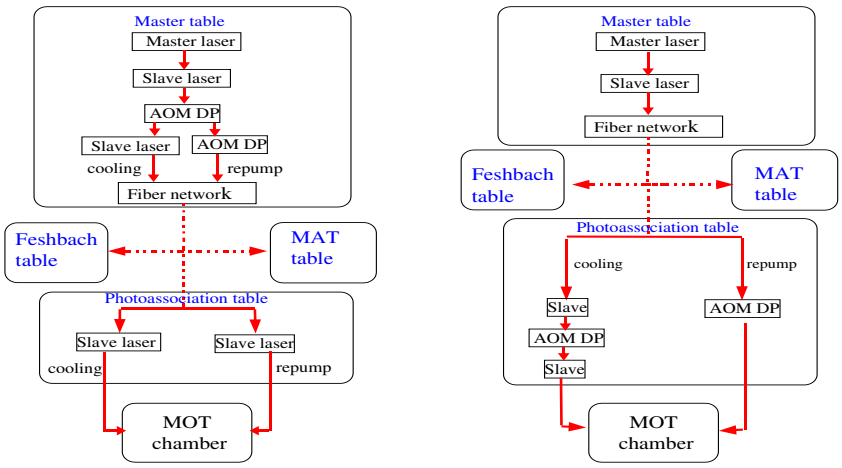

(a) Li (b) Rb

Figure 4.9: Flowchart summarizing the procedure for the creation of the a) Li and b) Rb cooling and repump light. The Feshbach and the MAT tables are other experiments in the QDG lab.

Light coming out from this master is used for the cooling as well as the repump light. As explained in 2.3.1, the hyperfine splitting of the ground state is small (228 MHz) such that both the cooling and the repump light can be obtained from the same master by shifting the frequency using an acoustic optic modulator (AOM). After passing an AOM double pass once, the light is split. One part, having the correct frequency for the cooling light, injects a slave, the other part passes another AOM doublepass being shifted further to the repump frequency and injectes another slave for amplification. Both the amplified cooling and repump light enter a fiber network and are split and transported to three different optical tables: the Feshbach table, which will be used to study Feshbach resonances, the MAT (miniature atom trap) table and the photoassociation table. Figure 4.9(a) summarizes the procedurce for creating the Li cooling and repump light.

For Rb the hyperfine splitting is much larger and the frequency range obtained by an AOM is not large enough to cover both cooling and repump frequencies. Therefore, two masters are required, one to generate the cooling light and one the repump light. As we want to cool both ^{85}Rb and ^{87}Rb,

there are in total four masters for the Rb light, two (cooling and repump) for ^{85}Rb and two for ^{87}Rb. Each Rb master injects a slave for amplification before the light is transported to the different experiments (see figure 4.9(b)).

The master table also contains a diagnostic setup for both Li and Rb in form of a Fabry–Perot interferometer where the output of each slave can be sent in order to check whether they are following the master laser.

The photoassociation table

Once the master light reaches the photoassociation table, both the Li and the Rb light undergo further amplification. There is one slave each for the Li cooling and for the Li repump light. The Li light does not need to be frequency shifted anymore, as this is done already done on the Master table by the two AOM doublepasses. The Rb cooling light after being amplified by one slaves is shifted to the correct frequency by doublepassing it through an AOM and is afterwards amplified again by a second slave. Since the repump light does not need to be very strong, it is not amplified and is directly frequency shifted by an AOM doublepass. In order to change the detuning of the cooling light or the repump light, we simply change the AOM frequency of these doublepasses. The Li light and the Rb light is mixed together with the help of a polarizing beam splitter (PBS) and then split into the three MOT axes and sent to the glass cell first passing quarter–wave plates properly oriented to obtain the right polarization. Since the optical pumping is very strong in Li, the Li repump light needs to be as strong as the cooling light and comes in from all six room directions. It contributes therefore to the cooling (but not trapping) process. The Rb repump, however, can be weak in comparison to the cooling light and is sent to the glass cell along only one axis.

4.3.2 Photoassociation laser

The wavelength of the photoassociation laser will be scanned starting from the asymptote of the first excited state ($2s + 5p_{1/2}$, 795 nm) to the red in order to map the energy levels of the excited state. The photoassociation light is produced by a Ti:Sapphire laser (Coherent 899-21) with a maximum output of 500 mW pumped by a 10 W Argon laser (Coherent Sabre). It is locked to a fiber comb similar to the one described in [38]. This measurement scheme has the advantage that we will know the frequency of the PA laser

within kHz and therefore be able to precisely calculate the location of the energy levels. The typical linewidth of the Ti:Sapphire laser is some MHz, after locking it to the fiber comb it will be in the kHz range. The frequency can be scanned by tuning the repetition rate of the fiber comb assuming that the Ti:Sapphire will follow. Once this locking is done, the photoassociation light will be mixed with the optical tweezer light and sent to the trapping cell using the same beam path.

4.3.3 Optical Tweezer

After cooling the atoms in a MOT, in order to create molecules, it is desired to transfer them to an optical trap (or dipole trap) in order to trap and further cool them. An optical trap is based on the dipole force which originates from the interaction between the light field and the induced dipole moment of the atoms. This force, in a strongly focussed laser beam, attracts atoms to the region of high light intensity and are therefore trapped at the position of the waist of the laser beam. The wavelength of this laser should be far red detuned, so that it is not in resonance with any relevant atomic transitions. In particular, we do not want to excite any created ground state molecules to the excited state. The potential curves in figure 3.5 indicate that the energy difference between the ground state asymptote and the minimum of the first excited state potential ($^3\Pi$) is $4279.7\,\mathrm{cm}^{-1}$. A fit of the potential around the minimum with the harmonic oscillator potential gives vibration frequency of $201.6\,\mathrm{cm}^{-1}$. The first vibrational level of this state therefore is located at $4582.7\,\mathrm{cm}^{-1}$ or 2182.1 nm above the ground state asymptote. It would be therefore favorable to have an optical tweezer laser which is red detuned to this value. Currently, in the lab, there is a fiber laser (IPG) emitting at a frequency of 1064 nm with a maximum output power of 20 W available. Being obviously not far enough to the red, it still can be used to trap the atoms. However, when it comes to accumulating molecules in the dipole trap, the wavelength of this laser will be a problem. Therefore, in the near future, another optical tweezer laser, probably also a fiber laser emitting at a wavelength red to 2182.1 nm will be purchased.

4.3.4 Ionization laser

Section 2.3.4 already explained our choice of ionization laser. It is a frequency doubled Nd:YAG laser (Continuum Minilite) emitting at 532 nm with a pulse

duration of 5.6 ns. For the ionization, the pulse energies are around 1 mJ. The laser sits on a small platform mounted above the ion pump and the beam is sent to the center of the trap cell using high reflective mirrors at 532 nm from the top at an angle as close as possible to the Brewster angle in order to minimize the reflections. The beam diameter is approximately 3 mm.

4.4 Magnetic coils

This experiment is mainly designated to produce molecules via photoassociation. In order to maximize the number of cold molecules produced, it is highly probable that the photoassociation is initiated on a loosely bound RbLi molecule, rather than a continuum state. The former has a much higher phase–space density. One proposal is to use a Feshbach resonance to produce this initial state. The study of Feshbach resonances requires much stronger magnetic fields (around 1 kG) and in opposite to the quadrupole field used to trap the atoms, it must be homogeneous. This can be obtained by running the coils in Helmholtz configuration. These high magnetic fields require a high current flow (25 to 30 A) through the coils which dissipates lots of heat. Therefore, instead of using normal air–cooled coils, a pair of water–cooled coils needed to be constructed.

4.4.1 Some theory on Helmholtz coils

In the Helmholtz configuration, a pair of identical coils are placed along a common axis separated by a distance equal to the radius of the coils. If equal current is sent through both coils in the same direction, this configuration produces a magnetic field which is spatially nearly uniform in a cylindrical region extending between the centers of the two coils. The magnetic field can be calculated by starting with the field produced by a circular current loop with the Biot–Savard law, expanding the field components into a power series and adding the contributios of two identical loops to get the field generated by a pair of coils. A more detailed derivation can be found in [40]. The result is:

$$
\begin{aligned}
B_z &= \mu_0 I \frac{R^2}{(D^2+R^2)^{3/2}} + \mu_0 I \frac{3}{2} \frac{R^2(4D^2-R^2)}{(D^2+R^2)^{7/2}} (z^2 - \rho^2/2) + \ldots \\
B_\rho &= \mu_0 I \frac{3}{2} \frac{R^2(4D^2-R^2)}{(D^2+R^2)^{7/2}} z\rho + \ldots
\end{aligned}
$$

where z is the position along the axis, B_z the magnetic field component along the axis, ρ the radial position, B_ρ the radial field component, μ_0 the permeability constant, I the current, R the radius of the loop and $2D$ their separation (see figure 4.10). Note that there are no third order terms, the next non–zero terms are of fourth order. Inserting the Helmholtz condition $R = 2D$, even the second order terms vanish and the fields are given by

$$
\begin{aligned}
B_z &= \mu_0 I \frac{8}{5\sqrt{5}R} + \ldots && (4.1) \\
B_\rho &= 0 + \ldots && (4.2)
\end{aligned}
$$

The radial component is zero, whereas the component along the axis is independent of z and the field therefore uniform to the third order.

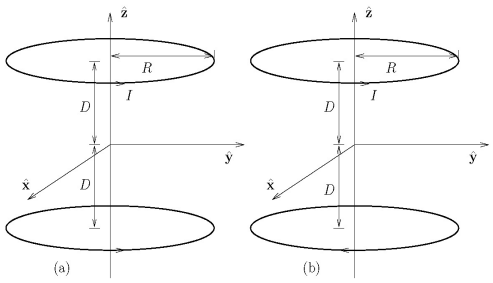

Figure 4.10: Geometry for a pair of coils in a) Helmholtz configuration, b) anti–Helmholtz configuration (taken from [40])

For the anti–Helmholtz configuration, the fields to the second order are given by

$$
\begin{aligned}
B_z &= \mu_0 I 3 \frac{DR^2}{(D^2+R^2)^{5/2}} z + \mu_0 I \frac{15}{24} \frac{R^2(4D^2-3R^2)}{(D^2+R^2)^{9/2}} (4z^3 - 6\rho^2 z) + \dots \\
B_\rho &= -\mu_0 I \frac{3}{2} \frac{DR^2}{(D^2+R^2)^{5/2}} \rho + \mu_0 I \frac{15}{16} \frac{R^2(4D^2-3R^2)}{(D^2+R^2)^{9/2}} (\rho^3 - 4\rho z^2) + \dots
\end{aligned}
$$

which gives for $R = 2D$ first order gradients of

$$\frac{\mathrm{d}B_z}{\mathrm{d}z} = \mu_0 I \frac{48}{25\sqrt{5}R^2} \tag{4.3}$$

$$\frac{\mathrm{d}B_\rho}{\mathrm{d}z} = \mu_0 I \frac{24}{25\sqrt{5}R^2} \tag{4.4}$$

Both $\frac{\mathrm{d}B_z}{\mathrm{d}z}$ and $\frac{\mathrm{d}B_\rho}{\mathrm{d}z}$ are independent of z. Furthermore, the gradient in radial direction $\frac{\mathrm{d}B_\rho}{\mathrm{d}z}$ is half as large as the gradient along the axis $\frac{\mathrm{d}B_z}{\mathrm{d}z}$.

These equations are valid for one single current loop. In order to get the field gradients generated by a coil consisting of n windings, an approximate value can be obtained by just multiplying with n and using the average radius of the loops. These equations are also valid only for infinitesimally thin wires and therefore only present an approximate value for both the magnetic field and the gradient.

The first coils constructed by Paul Lebel as described in [41] have a total amount of windings of 253 ± 2. Equation (4.2) predicts that these coils will generate in Helmholtz configuration a magnetic field of 834 G at a current of 25 A, where the average radius was used for R. A MatLab simulation which takes into account the finite size of the windings and sums over the contribution of all wire loops predicts a higher value of around 1 kG [41]. These coils were supposed to be used in the Feshbach experiment and I constructed another similar pair of coils. These coils have some less windings (225 ± 2) requiring therefore a higher current of 29 A in order to generate a magnetic field of 1 kG. For a current I, the dissipated power is given by

$$P_{\mathrm{diss}} = RI^2 \tag{4.5}$$

where the resistance R is calculated by

$$R = \frac{\rho l}{A} \tag{4.6}$$

with ρ being the resistivity, $l = 2\pi n\bar{R}$ ($\bar{R}$ is the mean radius) the total length and A the crosssectional area of the wire.

Using these equations, a dissipated power P_{diss} of the order of 1 kW for a current of 25 A is calculated for each coil. The required flow rate $\frac{\mathrm{d}V}{\mathrm{d}t}$ of the cooling water to cool one coil can be calculated by

$$\frac{\mathrm{d}V}{\mathrm{d}t} = \frac{P_{\text{diss}}}{c_w \Delta T \rho_w} \tag{4.7}$$

where c_w is the specific heat capacity of water ($4.19\,\frac{\text{kJ}}{\text{kg}\,^\circ\text{C}}$), ΔT the increase of temperature of the cooling water and ρ_w the density of water ($1000\,\frac{\text{kg}}{\text{m}^3}$). Allowing a temperature change of $2\,^\circ C$ of the cooling water, a flow rate of 6 l/min is calculated for each coil. Since the two coils are set up in series with the cooling water, the flow rate has to multiplied by a factor of two yielding 12 l/min.

4.4.2 Design and construction of the coils

[41] describes in detail how the first pair of coils was designed and constructed. This pair of coils was supposed to be used in the Feshbach experiment and another identical pair of coils was built. Since these coils have to be water–cooled, they sit in a PVC housing and 1/16 in phenolic spacer rods glued between every three layers of windings provide enough space for the water to circulate. Figure 4.11 shows a coil during the winding and gluing process.

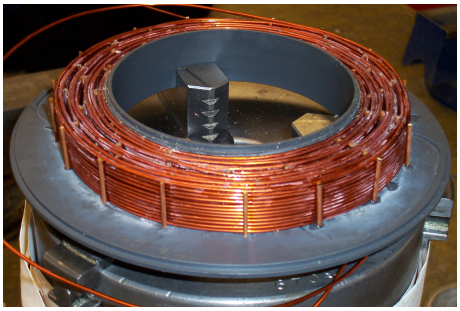

Figure 4.11: One of the MOT coils during the winding process

Kapton–coated coppe wire (16 gauge) was used as magnet wire, which offers thin, waterproof insulation. The wire enters and leaves the housing

through two holes which are attached to home–made PVC connectors connected by swagelocks to long PVC tubes letting the water in and out.
The PVC housing was sealed using purple primer to clean the surface and PVC cement to glue the two parts together. Testing the coils at the required flow rate did not cause any leaks. However, just to be sure, the coils were sent out for plastic welding to a local company (CPF Dualam) in order to make the seal secure. Since there is no water chiller available, we use filtered tap water for the cooling. After using the coils for some weeks, one of the coils cracked when the water was switched on which caused a water flood over the optical table. This accident was probably due to two reasons: first, the tap was turned on very quickly and second, there was a kink in the hose, both leading to a too high pressure which the seal could not hold. In order to quickly proceed with the experiment, these coils were replaced by the other pair of coils reserved for the Feshbach experiment. A water pressure regulator was then installed in order to protect these coils from a similar accident. Since we need to switch the coils off quickly and switch the polarity of one coil in order to toggle between Helmholtz and anti–Helmholtz configuration, a coil driver was constructed by the UBC electronics lab. It requires a digital input in order to turn the coils on and off and an analog input for the current control. For some experiments, the magnetic field must be turned off very quickly. Therefore, the ring down time of the induced voltage in a small pick–up coil positioned on top of the MOT coils was measured. We found it to be around 10 ms, which is rather long and needs to be improved.

4.5 Time–of–flight mass ion spectrometer

There are two ways of detecting the created LiRb molecules: trap loss or time–of–flight mass spectroscopy. Time–of–flight mass spectroscopy has the advantage of being able to detect even a small number of molecules and to distinguish between molecules of different masses. Therefore, a considerable amount of time was spent on the design and construction of a time–of–flight (TOF) mass spectrometer with sufficient resolution in order to separate a ^{85}Rb from a ^{87}Rb signal.

4.5.1 Some theory on time–of–flight mass spectroscopy

The principle of a TOF–spectrometer is fairly easy: the neutral atoms or molecules get ionized and, being positively charged, are accelerated by an electric field towards an ion detector. Due to their mass difference, they arrive at the detector after different time periods. This so called time–of–flight depends on the ion mass and therefore can be used to distinguish between different particles. A measure for the resolution of a TOF–spectrometer is the following expression

$$R = \frac{m}{\Delta m} \tag{4.8}$$

where m is the ion mass, Δm the mass difference to the next resolved mass, t the time–of–flight and Δt the difference between arrival times of the ion and the next resolved ion. In our case, separating a ^{85}Rb–signal from a ^{87}Rb–signal requires a resolution of $\frac{85}{2} = 42.5$ and separating a Li^{85}Rb–signal from a Li^{87}Rb–signal requires even a higher resolution of 45.5. Standard TOF–spectrometers consist of one acceleration region created by two field plates followed by a field free drift region. All ions starting at the same position (in direction of flight) gain the same kinetic energy while passing through the acceleration region. Ions of different masses enter the field free drift region therefore with different velocities, hitting the detector at different times. The resolution is limited by two issues: First, not all ions are produced at the same position. Therefore, ions of the same mass will have different velocities depending on their initial position. Second, all ions have different initial kinetic energies as well leading to different velocities. Both these effects cause some broadening of the signal. The resolution can be improved by using two acceleration regions as suggested by Wiley and McLaren [42]. The two acceleration regions are created by three field plates, as shown in figure 4.12. Here, $\vec{E}_s$ is the electric field of the first and $\vec{E}_d$ the electric field of the second acceleration region. s is the initial position of the ions , d the length of the second field region and D is the length of the field free drift region. The longer D, the better is the resolution of the spectrometer since the ions have longer time to get spatially separated from each other.

Changing E_s and E_d by adjusting the voltages applied to the field plates leads to a so called "space focussing". At a certain value of $\frac{E_d}{E_s}$ and D, all ions of the same mass being created at different positions are "focussed", meaning that they hit the detector at distance D at the same time. Ions starting closer to the first field plate, have to travel a longer way until they

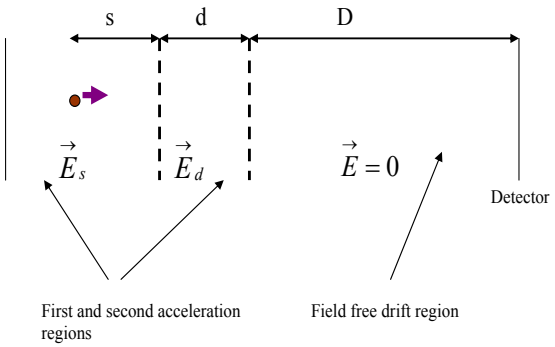

Figure 4.12: Mass spectrometer with two acceleration regions as suggested by Wiley and Mclaren [42]. The ions get accelerated in two stages leading to a so–called "space focussing" at a certain distance D, where all ions of the same mass but different starting positions hit the detector simultaneously.

reach the second plate, at the same time gaining more kinetic energy and therefore having a larger velocity. Ions starting closer to the second plate, enter the second acceleration region earlier but with smaller velocity. After some distance D the faster ions catch up with the slower ions, hitting the detector all at the same time. For a spectrometer with only one acceleration region, this distance is fixed at a value $2s_0$ [42], whereas it is adjustable for a spectrometer with two acceleration regions. However, the resolution is still limited by the initial kinetic energy distribution. In our experiment, the initial kinetic energy of the cold molecules or atoms is of the order of 10^{-8} eV, therefore this contribution to the signal broadening can be neglected.
The energy of an ion with charge q after passing both acceleration regions is

$$U = qsE_s + qdE_d \tag{4.9}$$

The flight time T can be calculated by summing over the times which the ions spend in the first acceleration region (T_s), the second (T_d) and the field free drift region (T_D):

$$T = T_s + T_d + T_D \tag{4.10}$$

T_s and T_d can be easily calculated from $\Delta t = \frac{\Delta v}{a}$ with Δv being the

change in velocity and a the acceleration experienced in the electric field given by $a = \frac{qE}{m}$. T_D is then given by $T_D = \frac{D}{v}$ with v being the final velocity of the ions after the second acceleration region. The result is

$$\begin{aligned} T_s &= \sqrt{\frac{2sm}{qE_s}} \\ T_d &= \frac{\sqrt{2m}}{qE_d}\left[U^{\frac{1}{2}} - (qsE_s)^{\frac{1}{2}}\right] \\ T_D &= \sqrt{\frac{m}{2(qsE_s + qdE_d)}}D \end{aligned}$$

For ions with initial position in the center of the first field region s_0, a total time–of–flight T of

$$T = \sqrt{\frac{m}{2U}}\left(2k_0^{\frac{1}{2}}s_0 + \frac{2k_0^{\frac{1}{2}}}{k_0^{\frac{1}{2}}+1}d + D\right) \tag{4.11}$$

is obtained, where $k_0 = 1 + \frac{d}{s_0}\frac{E_d}{E_s}$ [42]. The position of the space focus can be found by evaluating $\left(\frac{\mathrm{d}T}{\mathrm{d}s}\right)_{s_0} = 0$ and is

$$D = 2sk_0^{\frac{3}{2}}\left(1 - \frac{1}{k_0 + k_0^{\frac{1}{2}}}\frac{d}{s_0}\right) \tag{4.12}$$

4.5.2 Simulating the spectrometer

The challenging part of the design of the mass spectrometer was to design it such that it fits into the square cell without blocking any of the laser beams. Specifically, the problem was that the trapping cell has an inner diameter of only 20 mm and that cooling beams with diameter 2.5 cm come in at a 45 ° angle. This required the electrodes to be small (18×18 mm) and being far apart from each other (56 mm, 28 mm respectively). This geometry is shown in figure 4.13.

In order to that this configuration did not have excessive fringing fields, this configuration was simulated with the program SIMION [43], an ion optics simulation program that models 2D or 3D problems with electrostatic and/or magnetic potential arrays in a user defined workbench volume. At any point

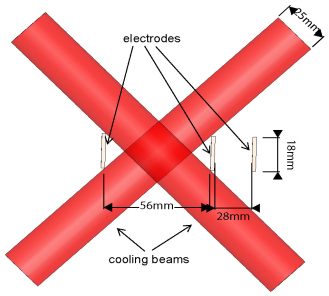

Figure 4.13: Geometry used to design the time–of–flight spectrometer. The electrodes have to be small and far apart from each other so that they fit into the trapping cell and do not block the cooling beams.

within this workbench, the electrostatic or magnetic field potential is calculated by solving the Laplace equation by finite difference methods with the electrodes (defined by the user) acting as boundary conditions. Ions can be released within the electrode model and their trajectories can be visualized and studied.

As a first step, three electrodes of the size and distance as in figure 4.13 were created in a 2D workbench suspended to free space 18.7 cm above a ground plate which represents the optical table top. The simulations were first done in 2D, since the setup (ignoring the table top) is cylindrically symmetric. Figure 4.5.2 shows the created electrodes and some equipotential lines (red lines) as obtained from SIMION.

The voltages for this simulation were set to 300 V for the first, 200 V for the second and 0 V for the third grid. For these voltages and our geometry, equ. (4.12) predicts a space focus at a distance D of 540 mm from the third electrode. When running the simulations, the layout of the vacuum system and therefore this distance was not known yet, so the simulations were run using this value for D and these voltages. The black line is the trajectory of a ^{85}Rb ion starting in the center of the first acceleration region. Obviously, the field is not homogeneous enough and the ion is deflected towards the table. In addition, there is the design issue of how to deliver the voltage to the electrodes, since any voltage line running to the electrodes is so close to the acceleration regions that it will influence the electric field. One solution

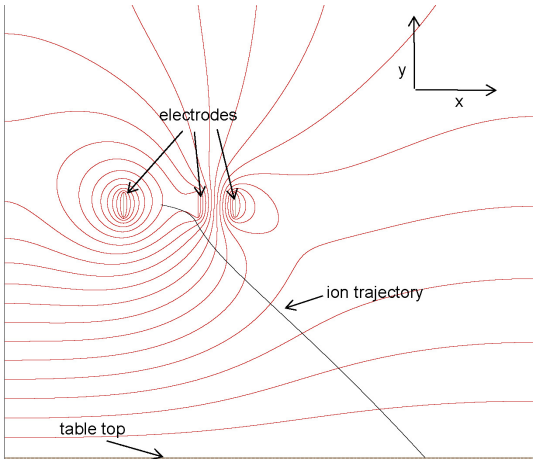

(a)

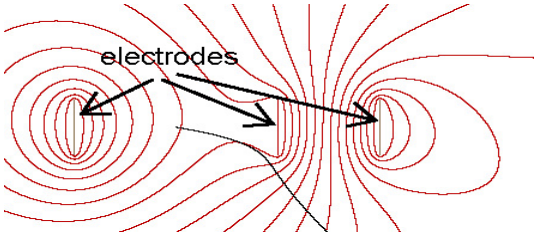

(b)

Figure 4.14: a) Result of a 2D simulation with SIMION for the electrode geometry shown in figure 4.13. The red lines are equipotential lines and the black line is the trajectory of a ^{85}Rb ion starting in the center of the first field region. b) Zoom into the electrode region for better viewing.

would be to run coaxial cables, therefore having an symmetric arrangement of four ground lines going to the electrodes. Another possibility would be to run hot lines carrying the high voltage for the grids (300 V and 200 V). Both configurations, however, would not improve the homogeneousness of the field and the ions would be deflected towards any of the voltage lines. A line which supports the homogeneousness of the electric field would be a line which is characterized by a potential which drops linearly in the region between the first and the last electrode. The effect of these new boundary conditions was modelled and investigated with SIMION. Since this configuration is not cylindrically symmetric anymore, a simulation in three dimensions was required. The result is shown in figure 4.15.

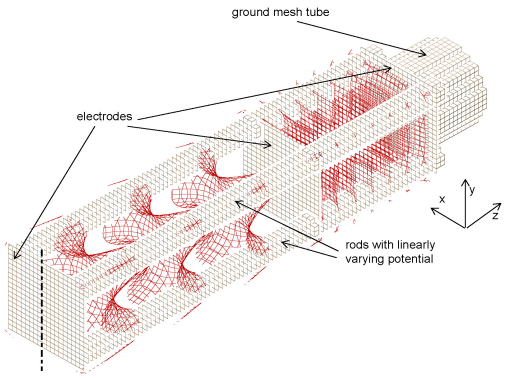

(a)

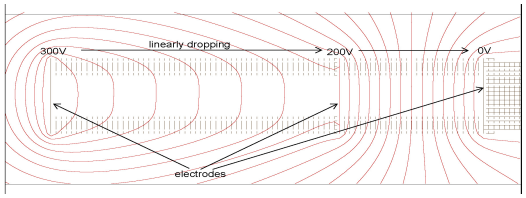

(b)

Figure 4.15: Result of a 3D simulation with SIMION. a) 3D view on the spectrometer model with some equipotential surfaces. b) 2D view on the plane going through the center (x–direction) parallel to the yz–plane.

Figure 4.15(a) shows the modelled spectrometer in 3D including the three electrodes and the beginning of the ground mesh tube. The field free drift region leading to the detector as well as the table top are not shown. Some equipotential surfaces are drawn and it is found that the field in the second acceleration region looks homegeneous, whereas the field in the first acceleration region looks distorted. Figure 4.15(b) shows a 2d view of a plane parallel to the yz–plane created by a cut along the dashed line drawn in figure 4.15(a). The field in the first acceleration region in the center region looks approximately homogeneous. Figure 4.16 gives another impression of the homogeneousness of the electric field, where the electric potential is plotted as a function of the position z as calculated by SIMION. It has linear behaviour in the second acceleration region and is zero in the field free drift region as desired. In order to investigate, if the field in the first acceleration is homogeneous enough in order to not deflect the ions, ions are released and their trajectories studied.

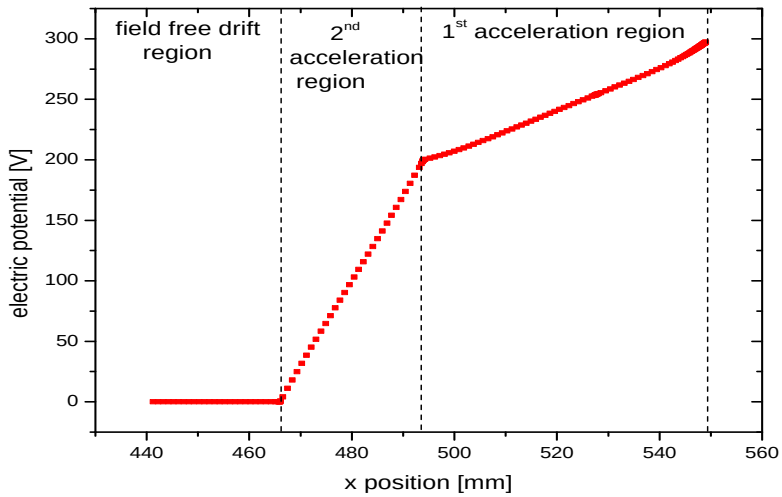

Figure 4.16: Electric potential as a function of z–position as obtained with SIMION. It drops approximately linearly in the two field regions and is zero in the field free region.

Following observations were made: it depends strongly on the starting

position if the ion hits the detector and the y–position is more critical than the x–position (due to the table top). The ions tend to be deflected down towards the table top. Ions starting in the region between 0.2 mm below and 1.8 mm above the center (in y–direction) hit the detector, all other ions are deflected too strongly. Figure 4.17 illustrates this behaviour. Figure 4.17(a) shows the ions' starting position and their trajectories within the acceleration regions. Figure 4.17(b) shows the ion trajectories in the region close to the detector. The lowest ion starts 0.2 mm below the center, the highest ion 1.8 mm above the center. This gives a starting region with an extension of 2 mm in y–direction (centered in x–direction) where the ions hit the detector. Since the MOT will have an diameter of 1 to 2 mm, this region should be large enough to obtain a signal on the detector.

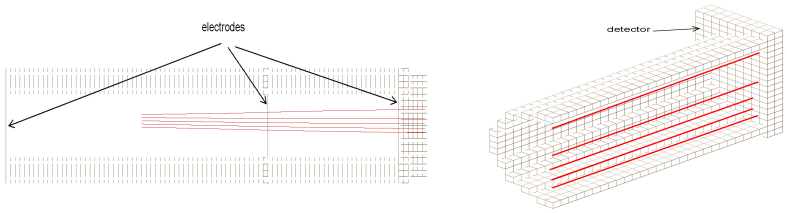

(a) (b)

Figure 4.17: Ion trajectories as obtained by SIMION for ions starting centered in x–direction but with different y–positions varying from 0.2 mm below to 1.8 mm above the center in y–direction.

Next, the resolution of this configuration was investigated. It will be limited by the distribution of initial z–positions. In order to study this effect, 1000 ions of each species with a gaussian distribution of initial z–positions (FWHM 1 mm), centered in x–direction and 0.5 mm above the center in y–direction were simulated and the time–of–flight distribution was recorded. The voltages were set to 300 V, 200 V and 0 V. Figure 4.18 shows the result for a drift region of $D = 420$ mm. This was the length chosen in the actual vacuum system.

The time separation between the $^{85}Rb^{+}$ signal and the $^{87}Rb^{+}$ signal is around 300 ns and the peaks have a broadening due to their initial distribution in z–direction of around 30 ns, which can be easily resolved by the detector. By adjusting the voltages [according to eq. (4.12)] such that the

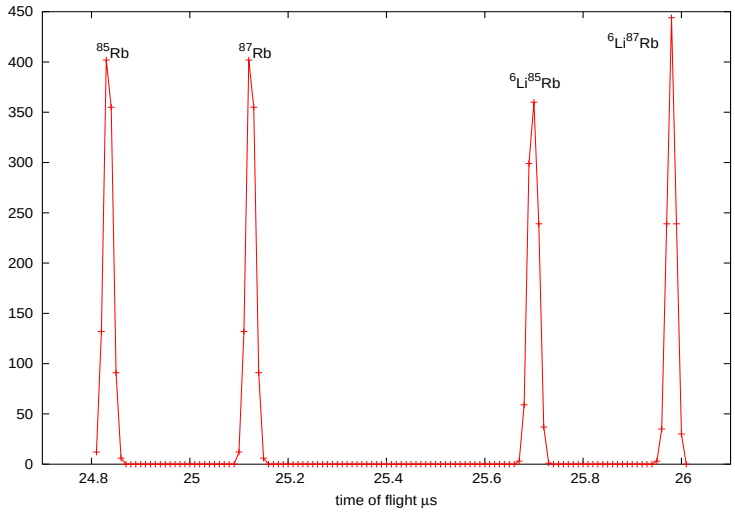

Figure 4.18: Time–of–flight signal obtained from simulations with SIMION.

space focussing happens exactly at this detector position, the resolution can be even improved. For this drift region, we expect a $^{85}Rb^+$ signal after 24.8 μs and a $^{87}Rb^+$ signal after 25.1 μs. The signal coming from Li ^{85}Rb and Li ^{87}Rb happens after 25.7 μs, 26.0 μs respectively, being also easily resolved. $^6Li^+$ and $^6Li_2^+$ (not shown in figure 4.18), being the lightest ions, are expected to hit the detector after 6.6 μs and 9.4 μs . All these simulations indicate that the resolution of this design will be sufficient enough and we decided to continue with the construction of the spectrometer.

4.5.3 Design, construction and testing

The final mass spectrometer consists of the accelerating grids, the electrical connections and the microchannel plate (MCP) detector. Figure 4.19(a) shows a drawing of the final design of the spectrometer and figure 4.19(b) a photograph of the spectrometer fitted into the glass cell.

The electrodes are circular stainless steel mesh of 13 mm diameter with 90 % transmission spotwelded onto a rectangular frame (18 × 18 mm) of the

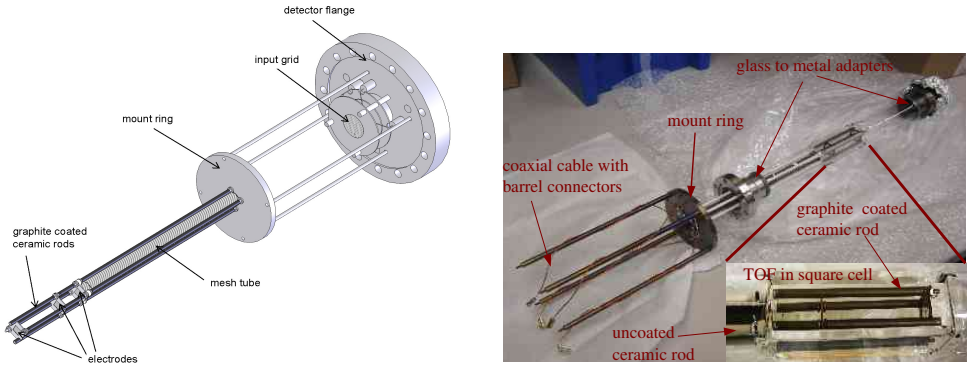

(a) Drawing of the time–of–flight mass spectrometer

(b) Photograph of the spectrometer inserted in the glass cell.

Figure 4.19: The time–of–flight mass ion spectrometer

same material. They are held by two pairs of threaded rods, each of them delivering the high voltage to one of the grids. For each grid, the voltage delivering pair of rods is connected to its frame by metal nuts, the other pair is insulated from it by ceramic bushings. The threaded rods are surrounded by ceramic rods. In order to realize the linearly varying potential, the ceramic rods were coated with graphite using a vacuum compatible graphite spray (Acheson Aerodag G). The goal was to make them conductive having a resistance as high as possible by coating them as thin as possible. Too few layers of graphite, however, do not give a very homogeneous coating. The highest and at the same time most homogeneous resistance achieved was around 100 kΩ for each rod. Such a high resistance causes a small current flow from the first grid to the second grid and from the second grid to the third ground grid dissipating only little power. A potential difference of 100 V gives a current of 1 mA through each rod dissipating 0.1 W of power. This current flow causes the potential along each rod to decrease linearly. Therefore, the surface of all four graphite coated rods had to be connected to each grid which was accomplished by wrapping a tiny wire around the graphite coating and spotwelding it onto the frame of the mesh. The third grid is connected to ground via the mesh tube which is attached to the mount ring held by four rods screwed into the detector flange.

The detector is mounted on a 6 inch conflat flange. This flange contains

two extra SHV feedthroughs which are connected to barrel connectors on the inside face of the flange. From there, thin vacuum compatible coaxial cables deliver the voltage to the threaded rods. The detector is a dual microchannel plate detector with a circular detection area of 18 mm diameter from Jordan TOF Products, Inc. A microchannel plate consists of tiny tubes (microchannels), in our case of 10 μm diameter with spacing of 12 μm. The detector consists of two microchannel plates mounted on top of each other in the so–called chevron configuration. Each microchannel acts as electron multiplier. Once an ion enters a microchannel, it sets free an electron which gets amplified in the microchannel in the presence of a strong electric field. Electrons exiting the first plate start an electron cascade in the second plate. The voltage difference between the two plates is usually around 1 kV. The gain achieved is $10^6 - 10^7$ for our detector, meaning that each ion hitting the detector produces $10^6 - 10^7$ electrons coming out of the bottom from the second plate. They are collected by an anode which is at a voltage more positive than the MCPs and matches the 50 Ω impedance of the signal cable. A voltage divider using high voltage resistors purchased from Caddock was built in order to apply voltage to each microchannel plate and the collecting anode. Using a single high voltage power supply with an output of -3 kV, a voltage of -2.2 kV is applied to the first plate, -1.2 kV to the second plate and -200 V to the anode. The electric circuit of the voltage divider is shown in figure 4.20(a) and a schematic of the MCP detector in figure 4.20(b).

Above the first MCP a ground grid is mounted which shields the drift region from the high voltage of the MCP ensuring that it is really field free. A mechanical shutter held by a rotary feedthrough mounted on one of the end flanges (see figure 4.3) to protect the MCP from the direct impact of the Li beam when the Li oven is on. Before inserting the whole spectrometer into the chamber for the final bake out, we checked if the potentials really vary linearly and it was found that they roughly do so, however, for a fixed position one pair of rods was slightly (5 %) more negative than the other one, for reasons which were not fully understood. We started the final bake out anyways, assuming that the electric field would still be homogeneous enough to obtain a strong enough signal from the ions.

When we reached the point to test the spectrometer, we made the following disappointing discovery: the resistances from the first grid to ground (instead of being in the kΩ range) was found to be 80 Ω, and from the second to ground 30 Ω making it impossible to apply a voltage difference between the two electrodes. At this point, the MOT experiment has been in use already

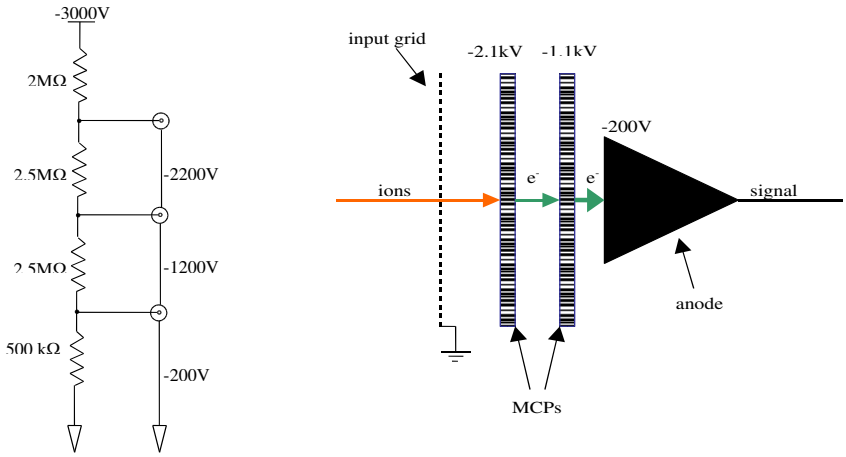

(a) (b)

Figure 4.20: a) Electrical circuit of the voltage divider; b) Schematic of the MCP detector

approximately for two months, and therefore the dispenser and the oven have been operated quite frequently, setting free fair ammounts of Rb and Li. Our explanation for these low resistances is that Rb and/or Li coated the graphite making it highly conductive. As reported in [44], it is found that, with Na, Li and Rb have the highest adsorption energy to graphite among all alkali atoms (1.21 eV for Li, 1.02 eV for Rb). We tried to run low current through the rods hoping that we could "clean" the rods by evaporating the Li and/or Rb. However, we did not want to run a too high current, since we were afraid of hot spots breaking the glass cell, since the rods are almost in contact with the glass cell. We did observe a drop in the MOT fluorescence, which might be either due to the dissipated heat or due to the fact that the magnetic fields produced by the current running through the coils disturb the MOT magnetic field yielding in a lower trapping efficiency.

Chapter 5

First Measurements and Results

This chapter starts with a brief theoretical overview of the loading of a MOT and then will present some first measurements on both the Li and Rb MOT. They include loading time measurements from which the number of trapped atoms and the background pressure can be estimated. Furthermore, in order to optimize the MOT in terms of maximizing the trap population, the number of atoms as a function of the detuning and the magnetic field gradient were investigated.

5.1 Loading a MOT

The number of atoms in a trap is determined by the balance between the capture rate into the trap and the loss rate from the trap leading to a simple differential equation describing the time dependence of the trapped atom number:

$$\frac{dN}{dt} = R - \frac{N}{\tau} \tag{5.1}$$

Here, N is the number of atoms, R is the rate at which atoms are captured from the background vapor, and τ is the loading–time constant determined by losses due to collisions. The inverse of the loading time $\frac{1}{\tau}$ gives the loss rate γ and depends both on collisions with background atoms as well as collisions with hot, untrapped Rb or Li atoms. The solution to this equation is

$$N = N_s(1 - \exp(-t/\tau)) \tag{5.2}$$

Here, $N_s = R\tau$ is the steady state number of atoms, which is the value for the number of atoms at which the capture and loss rates of the trap are equal. τ is the time constant for the trap to fill to its steady state value N_s and is also the average time an atom will remain in the trap before it is knocked out by a collision. For a given maximum capture velocity v_c the capture rate R can be calculated [48]:

$$R = \frac{1}{2} n v_c^4 V^{2/3} \left(\frac{m}{2k_\mathrm{B}T} \right)^{2/3} \tag{5.3}$$

where n is the density of atoms in the chamber, V the trapping volume and $\sqrt{\frac{2k_\mathrm{B}T}{m}}$ is the most probable velocity v_{mp}. v_c is the velocity at which the Doppler shift takes the atoms out of resonance by one linewidth, therefore is given by $(|\Delta| + \Gamma)\lambda/2\pi$. For a detuning of one linewidth, $v_c \approx 2\Gamma\lambda/2\pi$ which is $9.3\,\frac{\mathrm{m}}{\mathrm{s}}$ for Rb and $7.9\,\frac{\mathrm{m}}{\mathrm{s}}$ for Li. R is very sensitive to v_c because the stopping force decreases rapidely with velocity, once the Doppler shift gets so large that the atoms are out of resonance with both the laser beams.

5.2 The fluorescence imaging system

The fluorescence from the trapped atoms is imaged onto both a charge–coupled device (CCD) for viewing and a calibrated silicon photodiode for quantitative measurements. In our setup we needed a way to detect both the fluorescence light emitted by the Li atoms as well as the fluorescence light emitted from the Rb atoms. The detector had to be mounted about 30 cm away from the center of the trap cell to accommodate the optics belonging to the photoassociation beam path. Therefore, two lenses mounted on the beginning and the end of a cylindrical aluminum tube were constructed. Both lenses have a focal length of 75 mm. The first one is positionned such that the MOT is in its focus in order to collimate the fluorescence and the second one focusses the fluorescence back on the detector. In this manner, the image is not magnified and we do not have to worry if it fits on the detector surface. In order to separate the Li from the Rb fluorescence, a dichroic mirror is set up after the second lens. This mirror transmits the Li signal at 671 nm with an efficiency of 98 % and reflects the rubidium signal with an efficiency of 96 %.

A schematic of the fluorescence imaging system is shown in figure 5.1. Both the transmitted Li signal and the reflected Rb signal hit a silicon photodiode (Thorlabs SMIPD2B) with large detection area of 9 mm diameter. In front of each detector an interference filter is set up with a bandwidth of 5 nm which transmits only either Rb or Li light in order to compensate for the imperfection of the dicroic mirror.

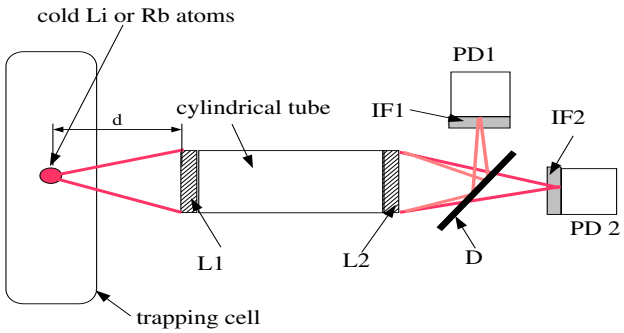

Figure 5.1: Schematics of the fluorescence imaging system: Two lenses L1 and L2 transport the images to two photodetectors PD1 and PD2. A dichroic mirror D and two interference filters IF1 and IF2 separate the Li from the Rb signal

5.3 Rb–MOT – Number of atoms and background pressure

The number of trapped atoms N is directly related to the fluorescence signal on the photodiode. To estimate N, the optical power P_{det} on the photodiode is fitted to the following expression:

$$P_{det} = \frac{hc}{\lambda}\frac{\Omega}{4\pi}N\gamma_{sc} \tag{5.4}$$

The first factor $\frac{hc}{\lambda}$ is the energy of one photon and the second factor $\frac{\Omega}{4\pi}$ is the solid angle subtended by the detector at the cloud. $\frac{\Omega}{4\pi}$ may be

approximated by the area of the circular lens L1 collecting the fluorescence divided by the area of the sphere of radius being the distance between the MOT and the lens:

$$\frac{\Omega}{4\pi} = \frac{\pi r_{\mathrm{L}}^2}{4\pi d^2} \tag{5.5}$$

where r_{L} is the radius of the lens L1 and d is the distance from L1 to the MOT. For our geometry ($r_{\mathrm{L}} = 11.4\,\mathrm{mm}$, $d = 75\,\mathrm{mm}$) this gives a factor of 0.00578. The scattering rate γ_{sc} is given by

$$\gamma_{sc} = \frac{\Gamma}{2}\frac{I/I_0}{1 + I/I_0 + (2\delta/\Gamma)^2} \tag{5.6}$$

where Γ is the lifetime of the excited state, I_0 the saturation intensity for the transition, I the total intensity of all six laser beams and δ the detuning. Table 5.1 contains numbers for the lifetime Γ, the saturation intensity I_0 and the wavelength λ of the transition for Rb as well as for Li

	I_0	$\Gamma/2\pi$	λ
Rb	$3.58\,\frac{\mathrm{mW}}{\mathrm{cm}^2}$	6.06 MHz	780.03 nm
Li	$2.54\,\frac{\mathrm{mW}}{\mathrm{cm}^2}$	5.87 MHz	671.00 nm

Table 5.1: Spectroscopic data for the saturation intensity I_0, the linewidth Γ and the wavelength λ for the cooling transition. (taken from [45], [46])

Figure 5.2 shows a loading curve of the Rubidium MOT with an exponential fit of the form of equation (5.2). From this fit, the photodiode voltage in the steady state region is determined to be 63.2 mV. Subtracting the background of 12.1 mV and using the calibration factor, a MOT fluorescence intensity of 122.3 nW is obtained. This value also accounts for 4% reflection loss per surface of the glass cell, the lenses and a loss of 2% on the dichroic beam splitter. This curve was taken for a detuning of 7.8 MHz or 1.3 Γ. The total intensity of the six laser beams was measured to be $53.1\,\frac{\mathrm{mW}}{\mathrm{cm}^2}$ which gives together with the saturation intensity for Rubidium $3.58\,\frac{\mathrm{mW}}{\mathrm{cm}^2}$ a saturation parameter I/I_0 of 14.8 and a scattering rate γ_{sc} of $1.5 \cdot 10^7$ photons/second yielding a number of trapped Rb atoms N of (equation (5.4))

$$N = 5.5 \cdot 10^6$$

From the exponential fit a loading time of 7.5 s is obtained. The loading time is a measure for the background pressure in the chamber. The lower the pressure, the smaller the loss rate and therefore the longer the loading time. The following expression was used to estimate the background pressure:

$$\gamma \approx n\sigma v_{mp} \tag{5.7}$$

Here, γ is the loss rate, n is the density of Rb background atoms, σ is the collisional cross section for Rb background atoms and v_{mp} is the most probable velocity. This will only give an approximate value, since first it is assumed that all atoms move at v_{mp} and second that there are only collisions with background Rb atoms. At room temperature assuming σ being $6.3 \cdot 10^{-13}\,\mathrm{cm}^2$ [47] gives a density n of $8.7 \cdot 10^6\,\mathrm{atoms/cm}^3$ which using the ideal gas law gives a pressure of $2.2 \cdot 10^{-10}$ torr.

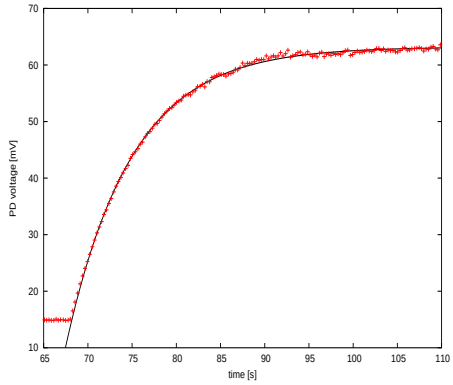

Figure 5.2: Rb loading curve for a detuning of $1.3\,\Gamma$ and a magnetic field gradient of $17\,\frac{\mathrm{G}}{\mathrm{cm}}$. The loading time is 7.5 s.

Figure 5.3 shows a picture of cold Rb atom cloud taken with the CCD camera. From this picture the size of the MOT can be estimated, and is found to be almost 2 mm.

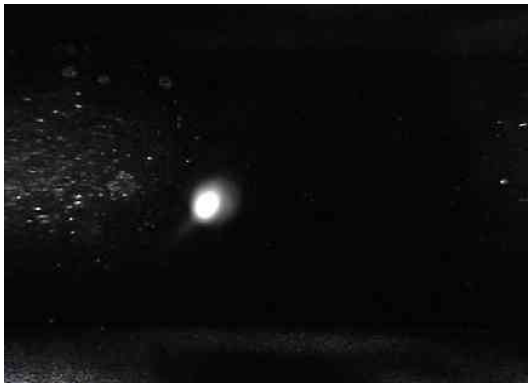

Figure 5.3: Picture of the cold Rb atom cloud taken with a CCD camera.

5.4 Rb–MOT – Changing the detuning

In the last section the fluorescence signal was used to estimate the number of atoms contained in the trap. The number of trapped atoms depends strongly on the detuning of the laser frequency from resonance since the detuning determines the maximum capture velocity v_c and the loading rate R scales with v_c^4 [equ. (5.3)]. We therefore studied the steady state population N_s as a function of the detuning δ in order to find the detuning which gives the highest number of trapped atoms. Different loading curves for different detunings were recorded. However, an increase or decrease in fluorescence when changing the detuning is not only due to the fact that the number of trapped atoms increases or decreases, but also due to the fact that the scattering rate [equ. (5.6)] changes. In order to eliminate this contribution and to get an absolute value for the number of atoms, the following procedure was used: A loading curve for a certain detuning δ_{load} (the "loading detuning") is recorded until it reaches its steady state. Then, the detuning is switched to a reference detuning δ_{ref} (in our case 7.8 MHz), which was kept constant for all measurements. Depending on if the scattering rate is smaller or larger for δ_{ref} than for δ_{load}, a sudden drop or raise in fluorescence followed by a loading or decay curve is observed. This jump in fluorescence is due only to the change in scattering rate. Three different cases appeared, all of them shown in figure 5.4.

In figure 5.4(a), δ_{ref} is smaller than δ_{load}, since the fluorescence increases when switching to δ_{ref}. More atoms are loaded into the trap at δ_{ref}. Figure

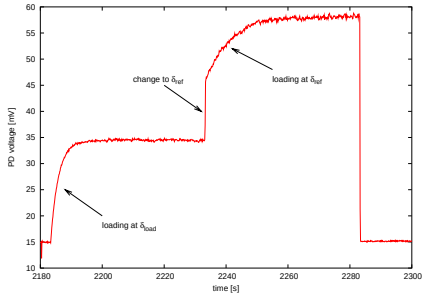

(a) Loading curve for a loading detuning δ_{load} of 23.5 MHz = 3.9 Γ

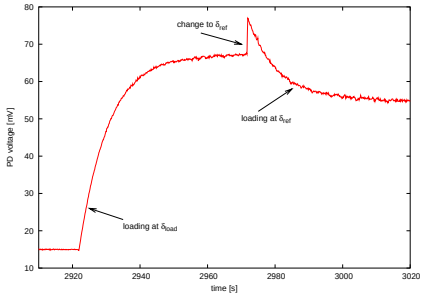

(b) Loading curve for a loading detuning δ_{load} of 12.3 MHz = 2.1 Γ

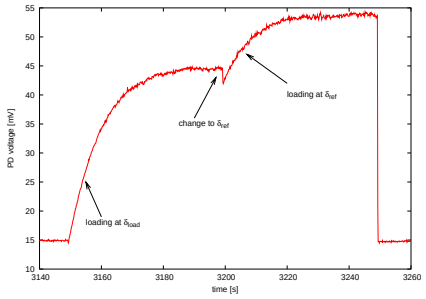

(c) Loading curve for a loading detuning δ_{load} of 5.58 MHz = 0.93 Γ

Figure 5.4: Loading curves for different detunings δ followed by curves recorded at a constant reference detuning of 7.8 MHz = 1.3 Γ

5.4(b) shows also an increase in fluorescence when switching to δ_{ref}, but is followed by a decay curve instead of a loading curve, meaning that less atoms can be held in the MOT at δ_{ref} than at δ_{load}. Figure 5.4(c) shows an example of a curve recorded in the case of δ_{load} being smaller than δ_{ref} characterized by a drop in fluorescence intensity, since the scattering rate decreases. As in figure 5.4(a) more atoms are loaded into the trap at δ_{ref}.
The number of atoms N was determined the following manner: Instead of using the fluorescence intensity in the steady state region of each detuning in order to calculate N, the intensity level which is reached immediately after switching to δ_{ref} is used. At this instance, the trap population has not changed yet and the detuning is the same for all measurements.
Therefore, fitting this intensity to the following expression, gives the number of atoms N for each detuning δ:

$$P_{det} = \frac{hc}{\lambda}\frac{\Omega}{4\pi} N \gamma_{sc}^{\delta_{ref}} \tag{5.8}$$

The result is shown is figure 5.5.

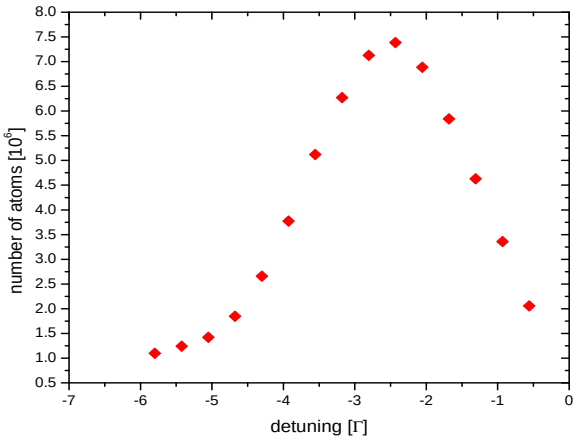

Figure 5.5: Number of trapped Rb atoms as a function of the detuning for a fixed magnetic field gradient $\frac{\mathrm{d}B_z}{\mathrm{d}z} = 16.8\,\frac{\mathrm{G}}{\mathrm{cm}}$.

The number of atoms N obtained by equation (5.8) is plotted as a function of the detuning δ. The dependency of the number of trapped atoms on the

detuning can be understood as follows. The loading rate R and therefore N scales with v_c^4 (equation (5.3)). At low values of the detuning, v_c and therefore the R is small yielding in a small number of atoms. With increasing δ, v_c and therefore N increases. For too large v_c, however, the distance it takes to slow the atoms down gets too large and and the atoms are not slowed within the size of the cooling beams. The optimum value of δ is at around 14.4 MHz which corresponds to -2.4Γ and is in good agreement with previous results [35], [49].

5.5 Rb–MOT – Changing the magnetic field gradient

The number of trapped atoms depends also on the magnetic field gradient. Therefore, in order to find the optimum field gradient, similar measurements to the ones performed on the detuning were done. At a fixed detuning of $13.4\,\mathrm{MHz} = 2.24\,\Gamma$, the current through the magnetic coils was changed. Again, each time after changing to a different current and recording a loading curve, the current was switched to a reference value of 2.84 A which corresponds to a gradient of $16.8\,\frac{\mathrm{G}}{\mathrm{cm}}$ for our coils and either a loading or a decay curve was observed. Switching to a reference current makes sure that for each measurement the Zeeman splitting and therefore the detuning is the same. Figure 5.6 shows the results of this measurement. The trap population is the highest for gradients between 10 and 15 G/cm. For small field gradients the trap is too shallow and atoms can easily escape. With increasing field gradient, the Zeeman splitting for an atom at a fixed position gets larger and the effective detuning δ_- therefore smaller (see figure 2.4). At higher field gradients, atoms are then resonant with the laser light at shorter distances from the trap center and therefore the volume where the atoms are trapped is smaller.

5.6 Li–MOT – Optimizing the number of atoms

The Li–MOT is found to be less dense than the Rb–MOT, because the atoms leaving the Li oven are fast, since we do not use a Zeeman slower to slow them down before cooling and trapping them. A photograph of the cold Li atoms is shown in figure 5.7. To the left of the atom cloud (inside the circle)

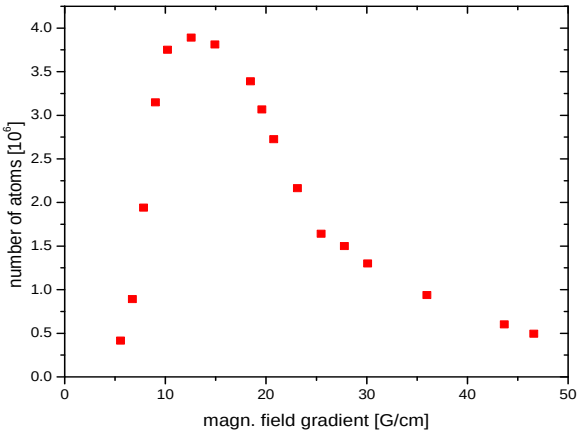

Figure 5.6: Number of trapped Rb atoms as a function of the magnetic field gradient for a fixed detuning of $\delta = 13.4\,\mathrm{MHz}$.

one of the mesh of the time–of–flight spectrometer can be seen.

Similar to our estimation of trapped Rb atoms, we first estimated the number of trapped Li atoms and the life time by recording loading curves by switching off and on the AOM on the Li light master table. Figure 5.8 shows three loading curves and their exponential fits taken for different detunings and magnetic field gradients.

The number of atoms was calculated using equation (5.4) in the same manner as for the Rb MOT. Table 5.2 shows the result.

gradient [G/cm]	detuning [MHz]	loading time [s]	number of atoms
11.8	15	1.71	$2.4 \cdot 10^5$
18.1	21	1.54	$2.5 \cdot 10^5$
23.6	24	1.90	$3.6 \cdot 10^5$

Table 5.2: Loading times and number of atoms for different magnetic field gradients and detunings for the Li MOT

As you can see from figure 5.8, the signal on the photodiode is much weaker with a bigger signal–to–noise ratio than the Rb signal and the number of atoms is smaller by approximately a factor of ten. In order to find out

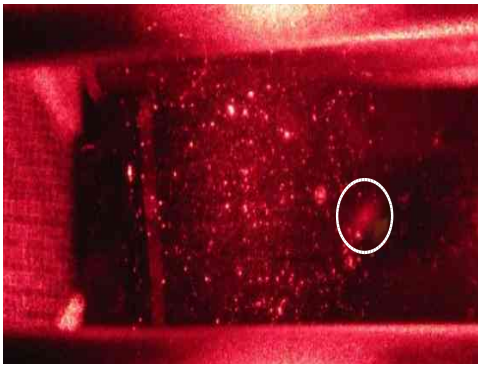

Figure 5.7: Photograph of the Li MOT.

which detuning leads to the maximum number of atoms, loading curves for different detunings for two magnetic field gradients were recorded in the same manner as was done for Rb. After recording a loading curve for a certain detuning δ_{load}, the detuning was switched to a reference detuning δ_{ref}, which lead to a sudden jump in fluorescence. This fluorescence level was taken as a measure for the number of atoms. The result is shown in figure 5.9, where this value is plotted against the detuning for two different field gradients. The red curve corresponds to a gradient of $11.8\,\frac{\text{G}}{\text{cm}}$ and the blue one to a gradient of $23.6\,\frac{\text{G}}{\text{cm}}$. Both curves have a maximum at a certain detuning, which is $15\,\text{MHz} = 2.6\Gamma$ for a field gradient of $11.8\,\frac{\text{G}}{\text{cm}}$ and $24\,\text{MHz} = 4.1\Gamma$ for a field gradient of $23.6\,\frac{\text{G}}{\text{cm}}$.

Note that for the smaller field gradient the maximum is reached at a smaller detuning, and starts dropping and detunings, where the curve for the bigger gradient still has a positive slope. This behaviour can be qualitively explained with the help of figure 2.4, which is shown slightly modified below (figure 5.10). The red line corresponds to the energy splitting for a field gradient of $11.8\,\frac{\text{G}}{\text{cm}}$, the blue line shows the splitting for a gradient of $23.6\,\frac{\text{G}}{\text{cm}}$. For a larger gradient, the splitting is larger and the energy levels shift closer to resonance with the by δ red detuned laser beam ($\delta_2 < \delta_1$). Therefore, it takes larger detunings δ to reach the point where the atoms are too much out of resonance to be effectively cooled.

As shown, the number of trapped atoms depends both on the detuning

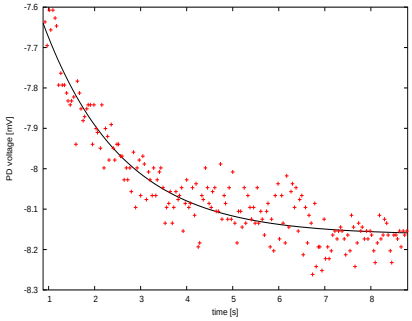

(a) $\frac{\mathrm{d}B_z}{\mathrm{d}z} = 11.8\,\frac{\mathrm{G}}{\mathrm{cm}}$, $\delta = 7.5\,\mathrm{MHz}$

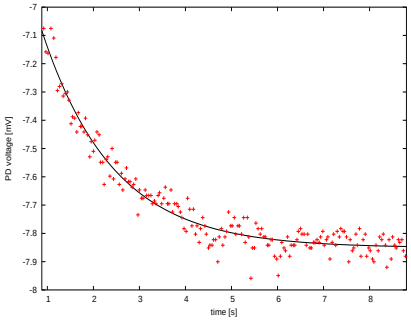

(b) $\frac{\mathrm{d}B_z}{\mathrm{d}z} = 18.2\,\frac{\mathrm{G}}{\mathrm{cm}}$, $\delta = 7.5\,\mathrm{MHz}$

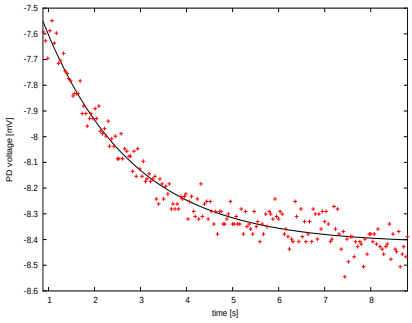

(c) $\frac{\mathrm{d}B_z}{\mathrm{d}z} = 23.6\,\frac{\mathrm{G}}{\mathrm{cm}}$, $\delta = 7.5\,\mathrm{MHz}$

Figure 5.8: Loading curves for Li for different magnetic field gradients and detunings.

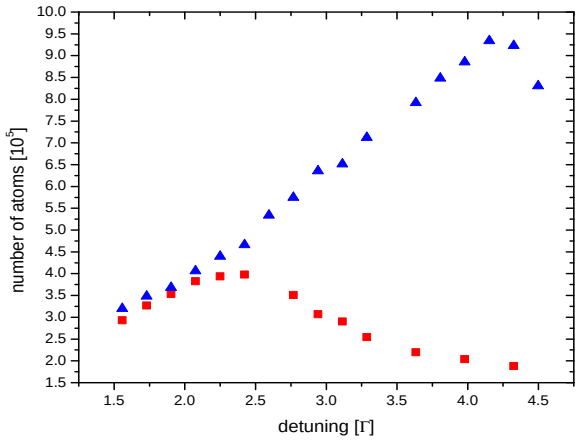

Figure 5.9: Number of trapped Li atoms as a function of detuning for two different magnetic field gradients. The red curve corresponds to a gradient of 11.8 $\frac{\mathrm{G}}{\mathrm{cm}}$ and the blue curve to a gradient of 23.6 $\frac{\mathrm{G}}{\mathrm{cm}}$.

and the field gradient and these two parameters are not independent from each other. Therefore, in order to find an optimum value, more measurements for both different detunings and field gradients must be performed, but the results obtained should be enough to get a rough idea which detunings and gradients are suitable. It is important to note, that for the Li MOT higher field gradients than for the Rb MOT are required in order to trap as many atoms as possible. Since the Li MOT is by virtue less dense than the Rb MOT, one should aim for a gradient which optimizes the Li MOT. This seems to be in the region (depending on the detuning) between 20 and 25 $\frac{\mathrm{G}}{\mathrm{cm}}$ which corresponds to currents between 3.3 and 6.4 A for our coils.

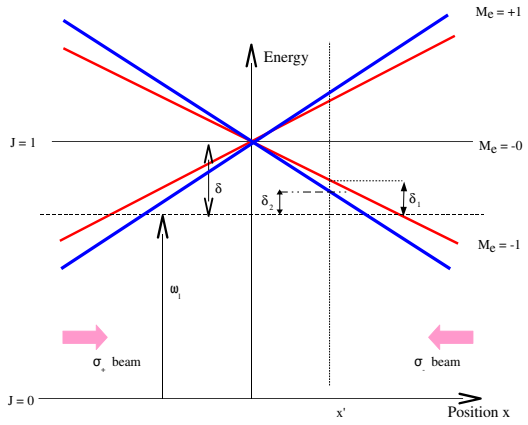

Figure 5.10: Zeeman splitting in a MOT for different magnetic field gradients.The red line corresponds to the Zeeman splitting caused by a field gradient of 11.8 $\frac{\mathrm{G}}{\mathrm{cm}}$, the blue line to 23.6 $\frac{\mathrm{G}}{\mathrm{cm}}$.

Chapter 6

Conclusion and Outlook

This work described first steps towards the creation of ultracold LiRb molecules. A dual–species MOT for cooling and trapping of Li and Rb atoms with all the necessary hardware was set up starting from an empty table. For my part, this included constructing a pair of water cooled magnetic coils, which, in Helmholtz configuration, are able to generate magnetic fields up to 1 kG necessary for studying Feshbach resonances. In anti–Helmholtz configuration, they are used as MOT coils. Furthermore, a vacuum system with a pressure of around 10^{-8} to 10^{-9} torr was built. This required careful cleaning of the vacuum components and a multiple step bake out. Before the bake out, tests of the atomic sources, the Rb dispenser and the Li oven were performed with the main motivation of outgassing them. In addition, work was completed on the system for direct detection of the LiRb molecules. Theoretical investigations on the LiRb potential curves were performed and an optimal wavelength of the ionization laser was determined. The ionization laser and optics in order to couple it into the trapping cell was set up. A time–of–flight mass ion spectrometer with high resolution was designed and constructed and inserted into the vacuum system. However, the graphite coating as described in section 3.5.3 caused some problems and it is not certain if the spectrometer in its current design will be able to work. For measurements on the dual–species MOT a two–colour fluorescence detection system was designed and built being able to detect both the Li and the Rb fluorescence. With the help of this detection system, loading curves on both MOTs were recorded in ordet to optimize the number of trapped atoms. It was found that this number depends both on the field gradient and the detuning. For Rb, for a detuning of 14 MHz a field gradient of 13 $\frac{\mathrm{G}}{\mathrm{cm}}$ is optimal, whereas the Li MOT

requires larger gradients of around 20 $\frac{\mathrm{G}}{\mathrm{cm}}$ to trap as many atoms as possible.

Unfortunately, the deadline of this thesis did not allow to take some photoassociation data, since the photoassociation light was not ready until the end of this work. Also, in order to do so, both the Rb and the Li MOT have to well overlap, which in the current setup, is quite hard if not impossible to achieve. The same set of optics is used to direct and polarize both the Rb and the Li towards the trapping cell which makes it impossible to move both atom clouds independently from each other. This might require setting up a second set of optics. Once the two clouds overlap well and the photoassociation light can be locked to the fiber comb for a sufficient long time, a photoassociation spectrum can be recorded by scanning the frequency of photoassociation laser and by recording the fluorescence. From the trap loss spectrum, the location of the energy levels can be obtained and having this information, the exact shape of the potential curves can be reconstructed. Since the lab is equipped with two Ti:Sapphire lasers there is the possibility of performing a two–color experiment. Here, the second Ti:Sapphire laser will be used to drive the molecules by stimulated emission to different ground state vibrational levels which will provide similar information on the ground state energy levels and potential curves. Furthermore, since the experiment is set up and ready to study Feshbach resonances, corresponding data will be taken in the near future as well. Once the optical trap works, the molecules can be accumulated and trapped and cold collisions in the molecular gas can be studied. Finally, LiRb molecules in the ground state are characterized by a large dipole moment and storing them in an optical lattice and observing a Fermi degenerate gas of polar molecules is another exciting goal of this experiment.

Chapter 7

Acknowledgements

I would like to express my gratitude to those who have contributed to the successful accomplishment of my thesis:

Dr. David J. Jones who gave me guidance, encouragement, and freedom during my time at UBC, Vancouver.

Dr. Kirk Madison, my second advisor. His commitment, enthusiasm, and competence are admirable.

Dr. PD Thomas Udem who kindly and without hesitation agreed to take the role of my official advisor at my home university in Munich.

Bastian Schuster, Dr. Bruce Klappauf, Swati Singh, Janelle van Dongen, Keith Ladouceur, Yifei Chen and Dr. James Booth for their kindness and willingness to help at all times of the day and for the fun we had in and outside the lab.

All other group members, Dr. Jie Jiang, TJ Hammond, and Rob Stead for the friendly atmosphere that they helped to create in the lab.

Brian Stene from the physics stores, Csaba Kodor and everyone else from the machine shop for always being so cheerful, friendly and willing to help.

My parents for their support during all the years of studying and for being how they are!

Bibliography

[1] T. Hänsch, A. Shawlow. *Opt. Commun.* **13**, 68 (1975).

[2] D. Wineland, H. Dehmelt. *Bull. Am. Phys. Soc.* **20**, 637 (1975).

[3] A. Ashkin. *Phys. Rev. Lett.* **40**, 729 (1978).

[4] W. Hofstetter, J. I. Cirac, P. Zoller, E. Demler, M. D. Lukin. *Phys. Rev. Lett.* **89**, 220407 (2002).

[5] M. H. Anderson, J. R. Ensher, M. R. Matthews, C. E. Wieman, E. A. Cornell.*Science* **269**, 198 (1995).

[6] A. Fioretti, D. Comparat, A. Crubellier, O. Dulieu, F. Masnou–Seeuws, P. Pillet.*Phys. Rev. Lett.* **80**, 4402 (1998).

[7] J. M. Sage, S. Sainis, T. Bergeman, D. DeMille. *Phys. Rev. Lett.* **94**, 203001 (2005).

[8] S. D. Kraft, P. Staanum, J. Lange, L. Vogel, R. Wester, M. Weidemüller.

J. Phys. B **39**, S993-S1000 (2006).

[9] C. Haimberger, J. Kleinert, M. Bhattacharya, N. P. Bigelow. *Phys. Rev. A* **70**, 021402 (2004).

[10] D. Wang, J. Qi, M. F. Stone, O. Nikolayeva, H. Wang, B. Hattaway, S. D. Gensemer, P. L. Gould, E. E. Eyler, W. C. Stwalley. *Phys. Rev. Lett.* **93**, 243005 (2004).

[11] M. Greiner, C. A. Regal, D. S. Jin. *Nature* **462**, 537 (2003).

[12] D. DeMille. *Phys. Rev. Lett.* **88**, 067901 (2002).

[13] H. J. Metcalf. *Springer Verlag* (1999).

[14] E. Raab, M. Prentiss, A. Cable, S. Chu, D. Pritchard. *Phys. Rev. Lett.* **59**, 2631 (1987).

[15] J. Dalibard and C. Cohen–Tannoudji. *J. Opt. Soc. Am. B* **6**, 2023–2045 (1989).

[16] P. J. Ungar, D. S. Weiss, S. Chu, E. Riis. *J. Opt. soc. Am. B* **6**, 2058–2071 (1989).

[17] P. Lett, R. Watts, C. Westbrook, W. D. Phillips, P. Gould, H. Metcalf, *Phys. Rev. Lett* **61**, 169 (1988).

[18] M. Kasevich, S. Chu *Phys. Rev. Lett* **69**, 1741 (1992).

[19] A. Aspect, E. Arimondo, R. Kaiser, N. Vansteenkiste, C. Cohen–Tannoudji *Phys. Rev. Lett* **72**, 203 (1994).

[20] J. S. Cohen, B. Schneider. *Journal of Chem. Phys.* **61**, 3230 (1974).

[21] J. O. Hirschfelder, W. J. Meath. *Adv. Chem. Phys.* **12**, 3 (1967).

[22] S. D. Kraft. *Formation, trapping and interaction of ultracold molecules*. PhD thesis. Albert–Ludwigs–Universitaet Freiburg. (2006)

[23] J. Doyle, B. Frieddrich, R. V. Krems, F. Masnou–Seeuws. *Eur. Phys. J. D.* **31**, 149 (2004).

[24] J. D. Weinstein, R. deCarvalho, T. Guillet, B. Friedrich, J. M. Doyle. *Nature* **395**, 148 (1998).

[25] H. L. Bethlem, G. Meijer. *Phys. Rev. Lett.* **83**, 1558 (1999).

[26] J. Weiner, V. S. Bagnato, S. C. Zilio, P. S. Julienne. *Rev. Mod Phys.* **71**, 1 (1999).

[27] W. C. Stwalley, H. Wang. *J. Mol. Spectrosc.* **195**, 194 (1999).

[28] H. R. Thorsheim, J. Weiner, P. S. Julienne. *Phys. Rev. Lett.* **58**, 2420 (1987).

[29] T. Köhler, K. Goral, P. S. Julienne. *Rev. of mod. Phys.* **78**, 1311 (2006).

[30] S. Singh. *Progress towards ultracold ensembles of Li and Rb.* Master thesis, University of British Columbia (2007).

[31] G. Igel–Mann, U. Wedig, P. Fuentealba, H. Stoll. *J. Chem. Phys.* **84**, 5007 (1986).

[32] M. Korek, A. R. Allouche, M. Kobeissi, A. Chaalan, M. Dagher, K. Fakherddin, M. Aubert–Frecon. *Chem. Phys.* **256**, 1, (2000).

[33] B. Bussery, Y. Achkar, M. Aubert–Frecon. *Chem. Phys.* **116**, 319 (1987).

[34] A. A. Radzig, B. Smirnov. *Reference data on atoms, ions and molecules*. Springer Verlag (1985).

[35] U. D. Rapol, A. Wasan, V. Natarajan. *Phys. Rev. A* **64**, 023402 (2001).

[36] A. Micheli, G. K. Brennen, P. Zoller. *Nature Phsics* **2**, 341 (2006).

[37] M. Lewenstein. *Nature Physics* **2**, 309 (2006).

[38] F. Adler, K. Moutzouris, A. Leitenstorfer, H. Schnatz, B. Lipphardt, G. Grosche, F. Tauser. *Opt. Expr.* **12**, 5872 (2004).

[39] B. Schuster. *Ultra-cold Rb and Li atoms in a Magneto-Optical Trap.* Diploma thesis, University of British Columbia, (2007).

[40] Meyrath, Todd. *Electromagnetic design basics of cold atom experiments.* (2001).

[41] Lebel, Paul. *Contributions to the UBC Quantum Degenerate Gas Lab.* Term report, University of British Columbia (2005).

[42] W. C. Wiley, I.H. McLaren. *Rev. of Scientific Instr.* **26**, 1150 (1955).

[43] SimIon 3D Version 7.0, Idaho Nation Engineering and Environmental Laboratory.

[44] K. Rytkönen, J. Akola, A. Manninen *Phys. Rev. B* **75**, 075401 (2007).

[45] D. A. Steck. *Rubidium 87 D Line Data* (2001).

[46] M. E. Gehm. *Properties of* ^{6}Li. (2003).

[47] T. A. Savard. *Raman induced resonance imaging of trapped atoms.* PhD thesis, Duke University (1998).

[48] H. Robinson, C. E. Wieman, C. Monroe, W. Swann. *Phys. Rev. Lett* **65**, 1571 (1991).

[49] K. Lindquist, M. Stephens, C. Wieman.*Phys. Rev. A* **46**, 1571 (1992).

I assure that I have composed the present work on my own and that I have not used other sources than indicated.

.....

Place, date of hand in signature of the author